Interrogation of cancer gene dependencies reveals novel paralog interactions of autosome and sex chromosome encoded genes

Anna Köferle[1,*], Andreas Schlattl[1,*], Alexandra Hörmann[1], Fiona Spreitzer[1], Alexandra Popa[1], Venu Thatikonda[1], Teresa Puchner[1], Sarah Oberndorfer[1], Corinna Wieshofer[1], Maja Corcokovic[1], Christoph Reiser[1], Simon Wöhrle[1], Johannes Popow[1], Mark Pearson[1], Barbara Mair[1,$], Ralph A. Neumüller[1,$]

[1] Boehringer Ingelheim RCV GmbH & Co KG, Doktor-Boehringer-Gasse 5-11, 1120, Vienna, Austria
* Equal contributing first authors
[$] Equal contributing last authors
[$] to whom correspondence should be addressed: barbara.mair@boehringer-ingelheim.com, ralph.neumueller@boehringer-ingelheim.com,

Abstract

Genetic networks are characterized by extensive buffering. During tumour evolution, disruption of these functional redundancies can create *de novo* vulnerabilities that are specific to cancer cells. In this regard, paralog genes are of particular interest, as the loss of one paralog gene can render tumour cells dependent on a remaining paralog. To systematically identify cancer-relevant paralog dependencies, we searched for candidate dependencies using CRISPR screens and publicly available loss-of-function datasets. Our analysis revealed >2,000 potential candidate dependencies, several of which were subsequently experimentally validated. We provide evidence that *DNAJC15-DNAJC19*, *FAM50A-FAM50B* and *RPP25-RPP25L* are novel cancer relevant paralog dependencies. Importantly, our analysis also revealed unexpected redundancies between sex chromosome genes. We show that chrX- and chrY- encoded paralogs, as exemplified by *ZFX-ZFY*, *DDX3X-DDX3Y* and *EIF1AX-EIF1AY*, are functionally linked so that tumour cell lines from male patients with Y-chromosome loss become exquisitely dependent on the chrX-encoded gene. We therefore propose genetic redundancies between chrX- and chrY- encoded paralogs as a general therapeutic strategy for human tumours that have lost the Y-chromosome.

Introduction

Paralog genes that fulfill similar functions provides a degree of robustness of gene regulatory networks to deleterious events[1–3]. These paralog genes arise as a result of gene duplications and subsequent divergent evolution[4,5]. Paralog redundancies are of interest to cancer biology, as tumour-specific processes like hypermethylation, mutations or copy number alterations can inactivate genes and thereby reduce the extent of genetic buffering. Genes whose loss is buffered in non-neoplastic cells by a paralog can thus become dependencies in tumours where the redundant paralog is absent. Examples for such paralog dependencies in cancer cells have been identified and validated before, and include *ENO1-ENO2*[6], *SMARCA2-SMARCA4*[7–9], *ARID1A-ARID1B*[10] or *STAG1-STAG2*[11,12].

In all validated cases, the tumour-specific loss of one paralog gene creates a specific dependency on a remaining paralog. Accordingly, therapeutic inhibition of the remaining paralog gene is assumed to be safe, because non-tumour cells still retain the genetic buffer to tolerate the inhibition without systemic side effects. Another advantage of tumour-specific vulnerabilities created by loss of a paralogous gene is the availability of a tractable biomarker; i.e. measuring loss of Paralog A in tumours allows to select patients that would respond to inhibition of the synthetic lethal Paralog B. Therefore, paralog dependencies represent a highly attractive concept for cancer drug target identification. However, a systematic understanding of cancer-relevant paralog dependencies is still elusive to date, although CRISPR-based combinatorial screens and bioinformatics discovery pipelines are beginning to shed light on the tumour redundancy map[3,13–20].

In addition to mutagenic processes such as gene silencing, point mutations or gene amplification, human cancers frequently lose large amounts of their genetic material during the process of tumourigenesis[21]. Deletions can involve one or multiple genes or, as is being appreciated, extend to loss of whole chromosomes, one of the most prevalent being loss of chromosome Y (LOY). Cancer incidence is generally higher in males[22,23], a fact that has been attributed to the general protective effect of the chrXX status in females that allows buffering of deleterious mutations[24,25]. LOY has been reported in ~93% of esophageal adenocarcinomas[26], ~12% of male breast cancers[27] and ~23% of urothelial bladder cancer samples[28]. Mosaic loss of chrY has also been observed outside of the oncology context, where it has been correlated with increased age[29–31]. LOY has been associated with a number of pathophysiological conditions, including clonal hematopoiesis and Alzheimer's disease[32,33]. Due to the plethora of disease states in which LOY occurs, strategies to eliminate cells involved in pathological conditions, including neoplastic transformation is clearly of general medical interest.

We set out to discover cancer-relevant paralog dependencies by an integrative approach of combining multiple -omics datasets in panels of human cancer cell lines. This analysis reveals 2,040 candidate paralog gene interactions, a subset of which we validate experimentally. Importantly, we uncover a sex-chromosome-specific set of genes that is functionally buffered between the X and Y chromosomes. We demonstrate that targeted depletion of the chrX-encoded gene in LOY tumour cell lines offers an attractive strategy to treat tumours that have lost chrY. In addition, these results provide a generalizable framework of how to eliminate putative pre-pathogenic LOY cells.

Results

CRISPR/Cas9 screens identify *CSTF2-CSTF2T* as a paralog dependency

We devised a set of proof-of-principle CRISPR screens to investigate the concept of cancer-specific paralog dependencies. We started by cataloging potential human paralog genes from Ensembl BioMarT, as defined by all genes with at least one other paralog in the same family without any further constraints on homology or family size. Most of the multi-gene families contain two to five paralog genes and the biggest class of genes are protein-coding genes (Figure 1a,b). A compact protein domain-focused CRISPR gRNA library[34] of ~10,000 gRNAs was generated to permit screening across multiple tumour cell lines. The library genes were manually curated to contain genes that are frequently deleted in human solid tumours,

including 460 unique paralog genes from 199 families. Loss-Of-Function (LOF) screens were then carried out across seven cancer cell lines (Hep 3B2.1-7, HuP-T4, MIA PaCa-2, NCI-H1373, NCI-H1993, NCI-H2009, PC-9) with annotated deep deletions (see Methods).

Paralog genes scoring as significantly depleted in our screens were cross-referenced across the different cell lines to understand whether any of their family members were annotated as deleted (Figure 1c, Supplementary Table 1). Accordingly, we found that *ATP4B* was specifically required in Hep 3B2.1-7 cells that harbor a deletion of *ATP1B2*. Both genes are subunits of potassium-transporting ATPases, but physical or functional interactions have not been described. Furthermore, we observed that NCI-H1993 cells were particularly sensitive to loss of *CSTF2*, likely due to a deletion of its paralog *CSTF2T*. *CSTF2* and *CSTF2T* encode the CstF-64 and CstF-64tau proteins respectively, that have partially overlapping functions in the Cleavage stimulation Factor (CstF) complex, a regulatory component of the mRNA cleavage and polyadenylation machinery[35–37]. We confirmed the sensitivity of *CSTF2T*-negative cells to depletion of *CSTF2* (Figure 1d, Supplementary Figure 1). Mechanistically, we observed that depletion of *CSTF2* leads to compensatory induction of *CSTF2T* in *CSTF2T*-proficient cells (Figure 1e), confirming previous reports describing that *CSTF2* and *CSTF2T* can regulate each other's expression[36,37]. This compensatory upregulation is not observed in *CSTF2T*-deficient cell lines (Figure 2f), providing a hypothesis for the dependency on *CSTF2*. Of note, *CSTF2* and *CSTF2T* are encoded by a single essential gene in yeast, *RNA15* (*YGL044C*)[38], suggesting that cellular viability might depend on the activity of both paralogues in mice and humans. In mice, the only apparent phenotype of *CSTF2T*-deficiency is male sterility which suggests that *CSTF2* and *CSTF2T* form a functionally redundant pair of genes with an essential function. Here, autosomally encoded *CSTF2T* is required in pachytene spermatocytes to overcome the lack of expression of X-encoded *CSTF2* due to meiotic sex chromosome inactivation[35].

In summary, this set of proof-of-concept screens - despite their limited scope - demonstrates that *bona fide* paralog dependencies are detectable using pooled LOF screens in cancer cell lines.

Bioinformatic identification of cancer-relevant candidate paralog dependencies

Due to the limited search space and number of paralog dependencies retrieved from our focused experimental approach, we decided to search for candidate interactions in a systematic manner, leveraging publicly available LOF and expression data from hundreds of cancer cell lines. We hypothesized that candidate genetic interactions between paralogous genes could be detected by looking at the relationship between expression of Paralog A and dependency on Paralog B. In essence, if low expression of Paralog A ("biomarker") was correlated with sensitivity to loss of Paralog B ("query"), this would identify a potential genetic interaction that could subsequently be evaluated. Depletion scores from complementary datasets[39] of pooled CRISPR and shRNA screens (AVANA[40], Sanger[41] and DRIVE[42]) and corresponding gene and protein expression data[43,44] for paralog genes were collected. Correlation coefficients and corresponding p-values between expression levels of biomarkers and depletion scores of queries for as many pairs within each paralog family where expression/depletion data were available were then calculated. This approach resulted in a large matrix of correlation tests, containing 14,064 unique genes (biomarkers or queries) and 108,092 unique biomarker-query pairs (Supplementary Table 2), hereafter called PaCT (Paralog Cancer Targets). The obtained correlation coefficients was then filtered via

116 a cutoff of 3*SD (standard deviation) and p-value < 0.05 to generate a hit set (Figure 2a,b; Supplementary
117 Table 2). Simulating the distribution of Spearman correlation coefficients by randomly assigning each
118 query to a gene from different family yields very few interactions at similarly strong correlations,
119 indicating the specificity of PaCT candidate pairs (see Methods; Figure 2c).

120 In contrast to other recent paralog studies, we did not limit the PaCT search space to paralog pairs by a
121 similarity cutoff or membership in a paralog gene family of a given (small) size[13,19]. An additional advantage
122 of PaCT is the ability to identify candidate interaction partners for genes that have not been targeted
123 themselves as queries, as long as expression data are available for them to act as biomarkers. Overall, of
124 3,084,147 possible pairs (including self-interactions) from 3,587 paralogue families, PaCT is blind to
125 2,975,741 pairs (2,795 genes), due to missing depletion and/or expression data for either query or
126 biomarker or both. This also includes pairs where information is available only for a single cell line and,
127 therefore, where no correlation can be calculated. From the remaining 108,406 paralogue pairs, 2,040
128 unique pairs (1.9%) were identified as significant interactions, and for 106,366 paralogue pairs (98.1%;
129 14,055 genes), we identified a non-significant correlation in our analysis (Figure 2d).

130 We then sought to identify possible differences between hit and non-hit paralogue pairs. Insufficient
131 variability in gene/protein expression and/or depletion scores across the cell lines could underlie low
132 correlation coefficients across our dataset. We investigated this for gene expression levels and depletion
133 scores from the AVANA dataset as an example. Indeed, we identified a small, but statistically significant
134 difference in variabilities for both modalities (p-value < 2.2×10^{-16}, Kolmogorov-Smirnov test) between hits
135 and non-hits (Figure 2e,f). We further hypothesized that sequence similarity between individual paralog
136 genes could impact the likelihood for an interaction between them. Indeed, based on Ensembl BioMarT
137 DNA sequence similarity, we observed a significant trend that genes involved in significant paralog
138 interactions exhibit higher similarity than those of non-significant pairs (Figure 2g).

139 Interestingly, significant pairwise candidate interactions are observed between paralogs in families of any
140 size (Figure 2h). Even though many candidate pairs are interactions within 2-member paralog families, we
141 scored significant correlations in larger families of up to 20 members or more. In smaller families, the
142 majority are positive correlations; with increasing family size, the balance shifts towards an even split with
143 negative correlations. On average (AVANA data), we identified 8.4% significant interactions per family
144 when family size is <= 10 that decreased to 1.4% for families containing more than 10 genes (Figure 2i,
145 Supplementary Figure 2 a,b). Finally, we looked at connectivity within paralog families and observed that
146 this varies widely (Figure 2j,k, Supplementary Figure 2c-f). Among the hit pairs, some queries and
147 biomarkers act as hubs, being involved in multiple or all significant interactions, independent of family
148 size. However, other candidates have a more uniform distribution, being identified in only a subset of hit
149 pairs. It remains to be determined what factors underlie these different degrees of connectivity.

150 As previously described by others[18,45], some gRNAs in the Sanger and AVANA datasets are promiscuous
151 and match to sites beyond the intended target. For PaCT, we used processed AVANA and Sanger scores
152 [40,41] and we confirmed (for the AVANA data as an example) that most genes had zero or one gRNA
153 excluded from the analysis for reasons identified by the investigators of the study (Supplementary Figure
154 2g; Supplementary Table 2). However, we confirmed previous observations that a sizeable fraction of
155 query genes (25%) had non-uniquely mapping gRNAs assigned to them (Supplementary Figure 2h;
156 Supplementary Table 2), constituting a potential source of false negatives [18,45] in our analysis.

157 Of the 2,472 candidate hit query-biomarker pairs (2,040 of which are non-redundant, involving 2,451
158 unique genes), 57% displayed a positive correlation between query dependency score and biomarker
159 expression. Most pairs (70%) were found using gene expression data, reflecting the greater robustness of
160 this dataset. We also included genes whose genetic dependency correlates with their own expression,
161 and 20% of our hits are indeed such "self-pairs". 20 of them have been previously described as CYCLOPS
162 (*c*opy number alterations *y*ielding *c*ancer *l*iabilities *o*wing to *p*artial loss) genes[46,47] that, when expressed
163 at low levels, are associated with greater sensitivity to further LOF. Similar to previous observations[47],
164 CYCLOPS genes are overrepresented among the significant hits identified by PaCT (20%), compared to
165 their representation among all potential interactions (13%), mirroring the high frequency of genomic loss
166 in cancer cell lines. In total, our PaCT analysis highlighted 370 unique candidate self-interactions.

167 The largest proportion of candidate hit query-biomarker pairs (46%) was detected in the AVANA dataset
168 – representing the largest and most comprehensive database in terms of cell lines included -, followed by
169 Sanger (37%) and DRIVE (17%). The covered cell lines and genes overlap to a certain extent, but each
170 dataset contains unique cell lines and genes, in addition to differences in methodologies for generating
171 LOF phenotypes (RNAi in DRIVE vs. CRISPR in AVANA and Sanger)[39]. Thus, it is not surprising that many
172 hits are found uniquely within one dataset or data domain (gene or protein expression; Figure 3a).
173 Nevertheless, 17% (432/2,472) of candidate pairs are recovered more than once, strengthening our
174 confidence in the PaCT approach. The largest overlap was observed between AVANA and Sanger positive
175 correlations pairs using gene expression as a biomarker, confirming those as high-quality candidates. To
176 illustrate the PaCT approach, Figure 3b shows examples of strong negative or positive correlations within
177 small paralog families along the diagonal, i.e. between expression and depletion of the same gene or
178 closely related paralogs, which are listed next to each other.

179 We complemented the PaCT approach by an additional analysis of the AVANA, DRIVE and Sanger data.
180 First, we classified cell lines as sensitive and resistant to depletion of a given query gene by k-means
181 clustering (k=3, leaving out the intermediate group). Then, we tested whether the expression of a given
182 biomarker gene was significantly different between the sensitive and resistant cluster. The most significant
183 negative correlation hits are almost exclusively self-interactions (Supplementary Figure 3a-c), consistent
184 with the notion of increased sensitivity to loss of highly expressed genes that might act as proliferation
185 drivers. On the other hand, the most significant positive correlation hits are pairs of paralogs
186 (Supplementary Figure 3a-c), supporting the hypothesis of functional redundancy and synthetic lethality
187 between those genes. Overall, the PaCT top hits also emerged as most significant in this analysis.

188 In order to characterize the PaCT hits, we investigated gene-centric parameters of the candidate pairs
189 (without self-interactions) that have been hypothesized by us and others to affect the likelihood of genetic
190 interaction between paralog genes[13,18]. We observed that some of our candidate interacting paralog pairs
191 (13%) are involved in protein-protein interactions (PPI) with each other, as annotated in BIOGRID[48]
192 (v4.3.196; Supplementary Figure 3d). We then checked the candidate pairs for homo- and heteromeric
193 interactions[3], where homomeric means the assembly of a protein with itself whereas heteromeric
194 paralogs assemble with each other. None of the candidate pairs is found on the (short) list of heteromers,
195 and ~3% of queries or biomarkers are annotated as homomers (Supplementary Figure 3d). We also
196 compared our list of candidate pairs to the Critical Paralog Groups (CPGs) defined by Modos et al.[49], i.e.
197 paralog groups that play important roles in signaling flow and pathway cross-talk. ~2% of PaCT pairs and
198 4-6% of query or biomarker genes are annotated as members of CPGs (Supplementary Figure 3d). Finally,

199 we investigated whether the candidate interacting pairs share the same common ortholog and whether
200 that ortholog is essential in different model organisms (Supplementary Figure 3e). While these numbers
201 provide a mere estimate, due to the caveats of ambiguous and incomplete ortholog mapping, we
202 expected and observed increasing fractions of common essential orthologs with increasing evolutionary
203 distance – from 0.4% in *M. musculus* to >5.5% in *S. cerevisiae*. Accordingly, the fraction of orthologs that
204 could not be mapped also increased, while the fraction of non-shared orthologs decreased.

205 Together, these characteristics of shared evolutionary origin and essentiality, or physical interaction,
206 describe some but not all parameters that underlie potential genetic and functional interaction between
207 paralogous genes. Recently, several groups have investigated paralog redundancy and interaction using
208 various computational and experimental methods[13–20]. We compared our PaCT candidates with their sets
209 of potentially interacting paralogs and recovered 12-67% of published pairs in our hit list (Supplementary
210 Figure 3f). Conversely, 15% of PaCT pairs are found in any other dataset. The published sets originate from
211 vastly different search spaces – from a few hundred experimentally tested pairs to computational
212 predictions of the complete interaction matrix of all annotated paralogs. Therefore, the variation in
213 recovery is not surprising and consistent with comparisons between the published datasets[13–20].

214 In addition, PaCT also identified several paralog dependencies that have recently been described,
215 including *SMARCA2-SMARCA4* or *SLC25A28-SLC25A37*[19]. We used CRISPR GFP-depletion assays to
216 experimentally validate the genetic dependencies on *FAM50A* in cells where *FAM50B* expression is low,
217 and on *VPS4A* in *VPS4B*-low cell lines (Figure 3c,d and Supplementary Figure 3g,h), two paralog
218 interactions that have recently been functionally characterized[19,50,51].

219 While most hits from dual-LOF screens and experimentally validated paralog dependencies rely on the
220 absence of Paralog A to detect dependency on Paralog B (or partial loss in a CYCLOPS interaction), PaCT
221 in principle identifies candidate interactions at any level of expression. To illustrate this, we calculated
222 the fraction of hit pairs with a relevant query depletion (AVANA or Sanger score < -0.5 or DRIVE score < -
223 3) in at least one cell line when the biomarker expression is low, medium or high (Supplementary Figure
224 3i). Indeed, the theoretical validation rate of candidate interactions is ~60% for all expression bins.

225 Overall, these findings validate PaCT as a complementary approach to retrieve validated as well as novel
226 candidates for interactions between paralog genes.

227

228 **_RPP25-RPP25L_ and _DNAJC15-DNAJC19_ are novel cancer-relevant paralog interactions**

229 In addition to previously described paralog interactions, we discovered several novel high-confidence
230 candidate dependencies, among them *RPP25-RPP25L*. RPP25 has been described as a component of the
231 RNase P and RNAse MRP ribonuclease complexes that process pre-tRNA and pre-rRNA sequences,
232 respectively[52–55]. Little is known about RPP25L, a role in tRNA or rRNA processing has not been functionally
233 validated. Sensitivity to loss of *RPP25L* was observed to be correlated with low expression of *RPP25* (Figure
234 4a, Supplementary Figure 4a,b). This was then experimentally validated using CRISPR depletion assays.
235 No depletion of *RPP25L*-targeting gRNAs was observed in cell lines that express *RPP25* (Figure 4b,c).
236 Overexpression of either *RPP25* or *RPP25L* in the sensitive U-2OS and KYSE-150 fully rescued sensitivity to

237 *RPP25L* LOF, demonstrating functional redundancy between these two paralogs (Figure 4d,
238 Supplementary Figure 4c). Interestingly, we observed a reduction in levels of endogenous RPP25L upon
239 ectopic overexpression of RPP25 (Supplementary Figure 4d,e) suggesting the existence of feedback
240 mechanisms that regulate the levels of RPP25L in response to changes in the abundance of its paralog
241 protein. In order to elucidate the underlying molecular mechanism of this paralog interaction, further
242 investigation of their role in pre-tRNA and pre-rRNA processing will be required.

243 Gene silencing is often accompanied by promoter hypermethylation[56]. We calculated the correlation of
244 methylation levels[44] of Paralog A with depletion scores of Paralog B and compared the methylation
245 correlation coefficients to the expression correlation coefficients from PaCT. As shown in Figure 5a,
246 (Supplementary Figure 5a,b; Supplementary Table 2) for some of the pairs, methylation status of Paralog
247 A could be a useful biomarker for dependency on Paralog B. In particular, we could also detect a
248 negative correlation between methylation and gene expression for multiple CpGs in the promoter
249 regions of *FAM50B* and *DNAJC15* (Figure 5b,c, Supplementary Figure 5c). Although correlation does not
250 necessarily imply causation, it is feasible that methylation could underlie low expression of the
251 biomarker paralog in these cases. DNAJC15-DNAJC19 has not been described as a paralog redundancy
252 before, therefore we set out to validate this interaction experimentally. *DNAJC15* expression levels
253 predict sensitivity of cell lines to loss of its paralog *DNAJC19* according to our PaCT analysis (Figure 5d,
254 Supplementary Figure 5d,e). We confirmed the sensitivity to *DNAJC19* knockout in cell lines that do not
255 express *DNAJC15* (Figure 5e) in CRISPR depletion assays (Figure 5f), including cells with high levels of
256 *DNAJC15* as negative controls. Cell lines that do express *DNAJC15* were predicted to be insensitive to
257 loss of *DNAJC19* and accordingly, *DNAJC19*-targeting gRNAs are not depleted from the pool of cells over
258 time. To conclusively demonstrate functional redundancy between the two paralogs, we overexpressed
259 *DNAJC15i* in the sensitive cell line NCI-H1975 and found that we could thereby rescue the dependency
260 on *DNAJC19* (Figure 5g and h).

261

262 **Paralog buffering between chrX- and chrY-encoded genes**

263 Loss of chromosomes have been reported to be frequently occur during cancer development[21]. Assessing
264 gene expression and copy number data across The Cancer Genome Atlas (TCGA), did not reveal obvious
265 bimodal distributions for any chromosome except chrY, suggesting that that whole chromosome loss is
266 not frequent enough to be detected in this manner across this dataset (Supplementary Figure 6a,b). As
267 described above, LOY has been associated with increasing age and noted in some cancers derived from
268 male patients[21,26–28]. In agreement with this, a bimodal expression distribution for chrY genes within 1.5%
269 of all male TCGA samples, was observed (Figure 6a). Binning samples by tumour purity shows that LOY is
270 more prevalent in samples with higher tumour purity, indicating that LOY could indeed happen more
271 frequently in cancers compared to adjacent normal tissue (Supplementary Figure 6c). Due to the absence
272 of matched non-tumour samples from TCGA, we used data from the Genotype-Tissue Expression (GTEx)
273 project to estimate the frequency of LOY in normal tissues. In corroboration of our hypothesis, at the same
274 99th percentile cutoff, no LOY was observed across normal samples GTEx (Supplementary Figure 6d).

275 These studies were further strengthened by analysis of the prevalence of LOY across cancer cell lines
276 used for the AVANA, DRIVE and Sanger screens. LOY was calculated as for the TCGA samples using copy

277 number and expression data and observed in 142 of 459 male cell lines (31% of male, 14% of all cell
278 lines) in our dataset (Figure 6b,c). These studies were supported by analysis of STR profiles for 455 cell
279 lines (46% of cell lines used for PaCT) and analysis of the amelogenin marker for presence or absence of
280 chrY (Figure 6i, Supplementary Table 3)(Figure 6i, Supplementary Table 3). We found that the previous
281 sex assignment was accurate, and LOY status was confirmed for all previously identified cell lines. We
282 further validated the sex chromosome status for a subset of cell lines by a PCR strategy (Figure 6j).

283 We next investigated whether PaCT retrieved any candidate interactions where the biomarker gene is
284 located on chrY to potentially exploit tumour LOY. Only 24 chrY genes were screened in the AVANA,
285 DRIVE or Sanger datasets, 22 of which are part of our paralog families. Interestingly, in four of these
286 pairs, the query genes are located on chrX: *DDX3X-DDX3Y*, *RPS4X-RPS4Y1*, *ZFX-ZFY*, *EIF1AX-EIF1AY*
287 (Figure 6d). These pairs also rank highly in the predictions by DeKegel *et al.*[13]. Notably, all four chrX
288 query genes are genes that escape X chromosome inactivation[57,58], and DDX3X is among a small set of
289 tumour-suppressor genes that escape from X-inactivation (EXITS genes)[59], where mutations occur more
290 frequently in male cancers and co-occur with LOY.

291 In order to validate dependency on the chrX paralog when the chrY paralog is not expressed (or chrY is
292 lost), we used CLIFF (*C*ell *L*ine d*IFF*erences)[60], a web application for the analysis of differences between two
293 sets of cell lines in terms of differential gene or protein expression, DNA copy number, gene signatures,
294 sensitivity to shRNA depletion or CRISPR gene knock-out and other parameters. First, we used k-means
295 clustering to classify cell lines as sensitive and resistant (k=3, leaving out the intermediate group) based on
296 their depletion scores in the AVANA dataset for each of the four chrX paralog hit genes. We then analyzed
297 these groups in CLIFF and looked for the parameters that are most significantly different between the
298 sensitive and resistant cell lines. As a control, we checked that the top gene in the AVANA category is the
299 respective query, i.e. *DDX3X* for the classification run on the *DDX3X* depletion scores (Figure 6e,
300 Supplementary Figure 6e-g). Other AVANA discriminators included some or all of the other chrX hit genes.
301 Conversely, chrY genes, with the respective paralog gene at the top, are the main discriminators based on
302 gene and protein expression, confirming LOY as a potential biomarker that predicts sensitivity to loss of the
303 four selected chrX genes (Figure 6e, Supplementary Figure 6e-g). As expected, LOY cell lines are therefore
304 enriched among the sensitive cell lines for all four chrX genes (Figure 6f, Supplementary Figure 6h-j; p-value
305 sensitive vs. resistant = 10^{-4} for all four genes, Fisher's exact test). Accordingly, AVANA depletion scores for
306 *DDX3X* (Figure 6g), *EIF1AX*, *ZFX* and *RPS4X* (Supplementary Figure 6h-m) are generally lower in LOY cell lines
307 than male cell lines. However, some male cell lines are also sensitive to loss of the chrX-encoded paralog,
308 indicating that the genetic buffering by the chrY-encoded gene might be incomplete in some contexts.

309 Consistent with these analyses, a Random Forest (RF) machine-learning model trained with chrY gene and
310 *DDX3X* paralog family gene expression data on the Sanger depletion dataset predicted sensitive and
311 insensitive cells for the AVANA dataset with an accuracy of 0.82. A variable importance analysis revealed
312 *KDM5D*, *DDX3Y*, *EIF1AY* and *RPS4Y1* expression as the top predictors for *DDX3X* sensitivity (Figure 6h).
313 Similar models for *ZFX* and *EIF1AX* were trained on Sanger data, predicted AVANA data with an accuracy of
314 0.715 and 0.82 respectively (Supplementary Figure 6n,o).

315 Genetic rescue experiments were performed to validate the putative functional redundancy between
316 chrX/Y-encoded paralogs. *DDX3X* dependency negatively correlates with the expression levels of *DDX3Y*
317 across a panel of >600 cancer cell lines (Figure 7a) i.e. across the AVANA dataset, low expression of *DDX3Y*-

318 but not other family members correlated with sensitivity to *DDX3X* depletion (Supplementary Figure 7a,
319 b). The *DDX3X-DDX3Y* functional redundancy was previously suggested in a hamster cell line[61] and Raji
320 cells[62] but has not been studied in the context of LOY. In HT-1080 cells, that possess chrY, whereas gRNAs
321 targeting *DDX3X* do not impact the proliferative capacity of these cells, rapid depletion was observed in
322 the context of a gRNA simultaneously targeting *DDX3X* and *DDX3Y* (Figure 7b). Importantly, the effects of
323 the *DDX3X-DDX3Y* dual-specific guide could be completely rescued by expression of gRNA-resistant cDNA
324 constructs for *DDX3X* or *DDX3Y*. Similar results were obtained for another male cancer cell line, HCT 116
325 (Supplementary Figure 7c). KURAMOCHI cells, derived from a female patient, are dependent on *DDX3X*
326 (Supplementary Figure 7d) demonstrating that buffering of the Y-encoded gene is *a priori* not part of the
327 genetic makeup. Finally, loss of Y-chromosome was confirmed in KNS-42 cells by PCR (Figure 6j). Rapid
328 depletion was observed with gRNAs targeting both *DDX3X* and *DDX3Y* simultaneously as well as gRNA
329 targeting *DDX3X* alone (Figure 7c). Ectopic expression of either *DDX3X* or *DDX3Y* completely reversed the
330 phenotype whereas a functionally unrelated X chromosome located gene X, *ZFX*, did not.

331 These findings were then extended to additional PaCT genes with a putative chrX/Y-encoded redundancy.
332 Sensitivity to *EIF1AX* correlates with the expression of *EIF1AY*, similar to *DDX3X-DDX3Y*, (Figure 7d,
333 Supplementary Figure 7e, f). LOY resulted in a strong dependency on *EIF1AX* (Figure 7f) whereas cells
334 retaining chrY were only sensitive to gRNAs simultaneously targeting *EIF1AX* and *EIF1AY* (Figure 7e).
335 Depletion could be reversed upon expression of gRNA-resistant cDNA constructs encoding for *EIF1AX* or
336 *EIF1AY* (Figure 7e, f). Similar results were obtained with gRNAs targeting *RPS4X* or *RPS4Y*, (Supplementary
337 Figure 7g). In addition to *DDX3X-DDX3Y* and *EIF1AX-EIF1AY*, *ZFX-ZFY* emerged as an additional functionally
338 redundant paralog pair from our PaCT analysis. Sensitivity of cancer cell lines to the loss of *ZFX* correlates
339 with the expression of *ZFY* and, less strongly, with *ZNF711* (Figure 7g, Supplementary Figure 7h,j). As the
340 sensitivity to *ZFX* loss-of-function is less pronounced in KNS-42 cells in the AVANA dataset[40], we turned to
341 female Cal-120 cells for depletion and rescue experiments. CRISPR/Cas9-mediated loss of *ZFX* resulted in
342 depletion of GFP- and gRNA-expressing cells. This phenotype could be rescued with gRNA-resistant cDNA
343 constructs encoding for *ZFX* or *ZFY*, validating the functional redundancy between the two proteins (Figure
344 7h).

345 In order to confirm that loss of chrY is the causative event in dependency on the paralogs encoded on
346 chrX we designed an approach to engineer removal of chrY (induced LOY, iLOY). Similar to published
347 approaches that have demonstrated loss of the targeted chromosome [63,64], a pool of 18 gRNAs targeting
348 chrY genes was introduced in HT-1080 cells ectopically expressing either *DDX3X* or *ZFX* [62,63] (Figure 7i). LOY
349 was validated by PCR (Figure 6j). Two independent clones were derived and subsequently treated with
350 gRNAs targeting *DDX3X*, *ZFX* and *EIF1AX*. Whereas no phenotype was observed in parental HT-1080 cells
351 (Figure 7b,f), LOY clones were sensitive to gRNAs for the chrX-encoded paralog genes. This sensitivity was
352 lost or reduced upon ectopic expression of corresponding gRNA resistant constructs, e.g HT-1080 iLOY
353 *ZFX* are sensitive to a gRNA targeting *DDX3X* whereas HT-1080 iLOY *DDX3X* are not (Figure 7j and
354 Supplementary Figure 7j).

355 Altogether, these data suggest that selective targeting of paralogs encoded on the X-chromosome, for
356 which genetic buffering with a chrY-encoded gene exists, might be a generalizable strategy to target LOY
357 tumours. The iLOY experiments validate the loss of chrY as the root cause for this dependency. To the best
358 of our knowledge, these are the first examples for synthetic lethal interactions between paralogs located
359 on the X and Y chromosomes.

360

361 **Discussion**

362 Exploiting distorted genetic buffering in human malignancies represents a promising therapeutic concept.
363 The clinical activity of poly ADP ribose polymerase (PARP) inhibitors in cancers with defects in the
364 homologous recombination-based DNA damage repair pathway[65–67] underlines this point. Paralog genes,
365 originating from gene duplication events, represent an additional subset of these general synthetic lethal
366 genetic interactions where tumour-specific loss of a paralog gene creates a therapeutically exploitable
367 dependency on the remaining paralog gene. In this study, we identified >2000 candidate paralog
368 dependencies relevant to human cancer. We have experimentally validated a subset of these paralog pairs
369 and provide evidence that genetic buffering between the sex chromosomes could provide an attractive
370 therapeutic strategy for human cancers of individuals that have lost the Y chromosome in malignant cells.

371 Our analysis was confined to cancer-relevant interactions that can be identified in the respective cell
372 lines used and genes targeted in publicly available CRISPR/RNAi LOF screens. Due to lack of equal
373 representation of different cancers within the datasets this could lead to a bias for certain tumour types.
374 As described, our discovery pipeline is also "blind" to certain other cases, including uniform expression
375 or depletion of a paralog across all screened cell lines. This is because expression-dependency
376 calculations rely on varying gene expression and depletion scores of one paralog gene across these cell
377 lines. Therefore, approaches like PaCT together with combinatorial genetic screens will further advance
378 our understanding of genetic redundancies. It will be interesting to determine if paralog interactions can
379 be tissue specific and if, within larger families, subsets of genes can have a greater or lesser functional
380 redundancy – a result suggested by our study. If true, this could hint towards the resistance of sub-
381 families and help to functionally annotate understudied paralog genes.

382 As the PaCT approach relies on publicly available screening data, the caveats of the original experiments,
383 such as suboptimal gRNA design in some instances, are carried over into our dataset. The *DNAJC15-*
384 *DNAJC19* example illustrates such a case, where all gRNAs in the public dataset also target a pseudogene
385 sequence. While our experimental validation uses independently designed gRNAs, a potential partial
386 function of the presumed pseudogene will have to be determined. Furthermore, additional
387 investigations will show whether *DNAJC15* and *DNAJC19* indeed both play a role in mitochondrial
388 morphogenesis, and whether *RPP25L* is a *bona fide* subunit of the RNase P/MRP complexes.

389 A number of mechanisms can underlie the paralog loss. In addition to mutation and deletion we provide
390 evidence that epigenetic mechanisms can also play a role. Validated paralog pairs *DNAJC15-DNAJC19* and
391 *FAM50A-FAM50B*, provide examples where high promoter methylation could, in part, account for
392 decreased expression of one paralog gene. This suggests that DNA hypermethylation in tumours could
393 expose novel vulnerabilities that could be exploited therapeutically. Future research will have to clarify if
394 vulnerabilities originating from DNA hypermethylation are stable enough to permit long-term treatment.

395 Our study revealed extensive genetic redundancy between the sex chromosomes. We identified four
396 candidate paralog dependencies (*EIF1AX-EIF1AY*, *DDX3X-DDX3Y*, *RPS4AX-RPS4Y1* and *ZFX-ZFY*) of which
397 we validated three experimentally. Our data suggest that cell lines originating from individuals with chrX
398 and chrY become sensitive to the loss of the chrX-encoded gene upon loss of chrY. While this concept

399 could in principle be exploited therapeutically to treat LOY tumours, premalignant states of mosaic LOY in
400 hematopoiesis or ageing-associated LOY, several hurdles would have to be overcome. It would be
401 important to ensure selectivity of the targeting therapeutic between highly similar paralogs. Although we
402 have not observed LOY across the GTEx dataset, it is possible that alternative mechanisms may also lead
403 to down-regulation of the chrY expressed paralog in normal tissues. While not explicitly addressed, recent
404 studies imply incomplete redundancy for *EIF1AX-EIF1AY* and *DDX3X-DDX3Y* in different contexts in
405 absence of LOY[68–70].

406 Overall, our study identifies cancer-relevant paralog dependencies and provides a framework for
407 validation and future discovery as further panels of functionally validated cancer cell lines become
408 available. While our PaCT approach currently addresses gene expression, deletion and methylation in the
409 paralog genetic space, the approach is generalizable and could be performed analogously for non-paralog
410 genes as queries, and mutations, passenger deletions or other tractable aberrations as biomarkers. We
411 envisage that this will identify additional testable hypotheses for targeted cancer treatment.

412

413 **Materials and Methods**

414 Cell culture

415 All cell lines and the respective media are listed in Supplementary Table 4. Cell lines were regularly
416 checked for mycoplasma, authenticated by STR profiling (Eurofins Genomics) and kept at low passage
417 numbers in humidified incubators at 37°C and 5% CO_2.
418

419 Generation of Cas9- and paralog-expressing cell lines

420 cDNA sequences for Cas9 and paralog genes were human codon-optimized, synthesized and cloned into
421 their respective vector backbone (Supplementary Table 4) at Genscript Biotech Corporation. Cells were
422 lentivirally transduced. Viral particles were generated using the Lenti-X Single Shot System (Clontech).
423 72 hours later, stable transgenic cell pools were selected using puromycin or blasticidin (see
424 Supplementary Table 4 for details).
425

426 CRISPR/Cas9 library design, cloning and virus production

427 The majority of genes in the gRNA library were manually selected from (i) paralog families of 2-5
428 members, (ii) genes frequently deleted in TCGA samples with a focus on deep deletions in lung
429 adenocarcinoma, lung squamous cell carcinoma, colon adenocarcinoma, liver hepatocellular carcinoma,
430 pancreatic adenocarcinoma, ovarian serous cystadenocarcinoma and prostate adenocarcinoma. gRNA
431 sequences were selected to target protein domains (annotated using PFAM domain identifiers) as
432 described[34], as well as control sequences for a total of 9574 gRNAs (Supplementary Table 1).

433 Pooled gRNA oligonucelotides (20-mer target sequences plus cloning adapters;
434 TGCTGTTGACAGTGAGCGCGTCTCTCACCG[20xN]GTTTGGAGACGCCTAGGATCGACGCGGACAACA; Twist
435 Bioscience) were PCR-amplified (0.1 ng DNA input, 24 parallel reactions, 15 cycles). Pooled reactions
436 were purified using the QIAquick PCR purification kit (Qiagen) and digested with BsmBI. The vector
437 backbone (lentiviral vector coexpressing sgRNA, GFP and NeoR, similar to sgETN[71]) was prepared by
438 BsmBI digestion, dephosphorylation and purification as above. Ligation was performed in 14 parallel
439 reactions using T7 ligase and remaining uncut backbone was removed by BsmBI digestion. Ligation
440 products were purified by phenol extraction, transformed into MegaX DH10B T1 electrocompetent
441 bacterial cells (Invitrogen) following manufacturer's protocol and plated on LB/Ampicillin plates.
442 Colonies were combined and maxi-preps were performed at ~7000x colonies per sgRNA.

443 Lentivirus was produced in 293T-Lenti-X cells (Clontech) using 10 µg of library DNA and Ready-to-use
444 Lentiviral Packaging Plasmid Mix (Cellecta, 0.5 µg/µL) per 10 cm dish (20 dishes in total). 293T-Lenti-X
445 were plated without antibiotics and transfected the next day using Lipofectamine LTX & Plus (Thermo
446 Fisher). Medium was changed after 7 h of incubation and viral supernatant was harvested after 48 h.
447 Virus titration was carried out individually for each cell line using three different amounts of viral
448 supernatant in the presence of 8 µg/mL polybrene. Transduction efficacy was evaluated 72 h after
449 infection by measuring GFP expression by flow cytometry.

450 Primer sequences are listed in Supplementary Table 4.
451

452 CRISPR/Cas9 screens

453 Cas9-expressing cell lines were transduced with the sgRNA library at a multiplicity of infection of ~0.3 in
454 the presence of 8 µg/mL polybrene. To this end, 44 x 10^6 cells were cultured in four or more T175 flasks
455 for 12/18 population doublings, representing 1000-fold library coverage. Cell numbers were adapted
456 according to measured GFP percentage after initial infection. From a pellet of the respective cell number
457 at the end point, genomic DNA was isolated using the QIAamp DNA Mini Kit (Qiagen). Amplicons around
458 the sgRNA sequences were PCR amplified (1 µg input per PCR reaction, 29 cycles) with barcoded
459 primers. The total amount of genomic DNA input was calculated by dividing the used total cell number
460 by the assumed value of 6 pg genomic DNA per cell. PCR products were purified using the QIAquick PCR
461 purification kit (Qiagen) and a 2% agarose gel using the QIAquick gel extraction kit (Qiagen). In a second
462 PCR, 10 ng of the purified product per reaction were amplified (5 cycles). The pooled PCR products were
463 purified using the QIAquick PCR purification kit. 50 ng of amplicons were used for the library generation
464 with the TruSeq Nano DNA Library Prep kit for NeoPrep (Illumina). The sequencing was conducted on a
465 HiSeq1500 (Illumina) in rapid mode with the paired end protocol for 50 cycles. For the 7 cell lines (MIA
466 PaCa-2, Hep 3B2.1-7, NCI-H1373, NCI-H1993, NCI-H2009, PC-9, HuP-T4) total read counts ranging from
467 3.1M to 41.6M were generated. Primer sequences are listed in Supplementary Table 4.
468

469 CRISPR/Cas9 library quality control and screen analysis

470 For the plasmid library, 20 million reads were generated and the gRNA representation was tested for
471 uniformity. gRNA counts ranged from 50 to 8708 reads (25th percentile: 983; median: 1682; 75th
472 percentile 2560 reads). For screen analysis, we used the 'mageck test' function of the MAGECK tool
473 (version 0.5.6)[72] to determine the log2-fold-changes and significance estimates (p-values, FDR) for gRNA
474 representation differences between any of the 7 cell lines and those observed in the plasmid library
475 using the following parameters: "mageck test --norm-method control --gene-lfc-method median".

476 To further assess the technical quality of the screens, we overlapped the library with known core-
477 essential (n=625) and never-essential (n=1344) genes constructed from genome scale screens. We found
478 that 307 and 596 gRNAs targeted a subset of the core- and never-essential genes, respectively. We
479 observed a good separation of both guide sets (strictly standardized mean difference < -0.9) and a
480 strong enrichment of core-essential genes in the top depleted genes (AUC > 0.9). Both quality metrics
481 were calculated based on log2-fold-changes from the comparison to the gRNA representation in the
482 plasmid library.

483 To compensate for the variable effect sizes from the different cell lines, we scaled all gene-level log2-
484 fold-changes such that the median log2-fold-change of all never-essential and core-essential genes
485 where set to 0 and –1, respectively. We call this scaled log2-fold-change escore (essentiality score).

486 For hit calling, we selected genes that were specifically depleted (cutoffs for escore < -0.4 and FDR < 0.1)
487 in cell lines that harbor a deletion of a member of the same paralog family (absolute copy number = 0
488 and log2 relative copy number < -1).
489

490 TCGA data

491 For gene expression data, the GDC Data Portal's interface (https://portal.gdc.cancer.gov/) was used to
492 compile all data files that mapped the fields “Program” = “TCGA”, “Data Type” = “Aligned Reads”,
493 “Experimental Strategy” = “RNA-Seq”, and “Workflow Type” = “STAR 2-Pass”. Using the GDC Data
494 Transfer Tool, the data was transferred and pre-processed using samtools[73] collate and fastq to generate
495 FASTQ files, containing the unmapped reads. All samples were subsequently processed with a
496 harmonized RNA-seq pipeline[74].
497 TCGA SNP6 copy number segmentation data was downloaded from NIH GDC
498 (https://portal.gdc.cancer.gov/) on December 3 2018. The segmentation information was obtained from
499 the files *nocnv_grch38.seg.v2.txt. Gene-wise copy numbers were determined by overlapping the
500 segmentation information with Ensembl v86 gene annotation. If a gene was covered by a single
501 segment, the copy number of the segment was assigned to the gene. If a gene was covered by multiple
502 segments, a weighted average copy number was computed based on the size of the overlap between
503 the gene and each segment. Relative copy numbers <= 1.0 were considered as “deep deletion”.
504 The R package TCGAbiolinks (v2.5.9)[75] was used to extract sample and patient information for TCGA
505 samples by using a custom-made R script.
506 The sample cohorts COADREAD, FPPP, GBMLGG, KIPAN, and STES were excluded.
507 Data for TCGA methylation loci plots were downloaded from http://www.bioinfo-zs.com/smartapp/[76].
508 Gene expression levels (log2(TPM)) were plotted against methylation levels of CpGs belonging to islands
509 located in promoter regions of genes of interest.
510

511 Cancer Cell Line Encyclopedia (CCLE) data

512 Cell line names and descriptions (including sex) were taken from the provider’s cell-line data sheet. If a
513 cell line was available from various vendors, the cell-line name was taken from the top rank in a
514 hierarchy of vendors in the following order: ATCC, DSMZ, ECACC, JCRB, ICLC, RIKEN, KCLB.
515 For gene expression, raw FASTQ data for all CCLE cell lines[44] were downloaded via the European
516 Nucleotide Archive (accession number PRJNA523380). All data were processed identically to TCGA data
517 as described above.
518 For copy number determination, SNP6 CEL files were downloaded from https://cghub.ucsc.edu/ in
519 October 2012. Relative copy number segments were computed using the R packages aroma.affymetrix
520 (v3.1.0)[77] and Rawcopy (v1.1)[78]: SNP6 data were processed with the AROMA method CRMA v2, where
521 the 50 samples with the least amount of copy number alterations based on Rawcopy were used to
522 calculate the reference intensities. This was followed by CBS segmentation. Afterwards, the copy
523 number segments were overlapped with Ensembl v86 gene annotation as described for the TCGA data
524 in order to obtain gene-wise relative copy number values. “Deep deletion” status was assigned as for
525 TCGA data. Absolute copy number segments were computed using PICNIC version c_release 2010-10-
526 29[79] with reference files adapted for reference genome hg38 and default parameters. The resulting
527 segments were overlapped with Ensembl v86 gene annotation as for TCGA data in order to obtain gene-
528 wise absolute copy number values.
529 Methylation[44] data are 'CCLE_RRBS_TSS1kb_20181022.txt.gz', downloaded from
530 https://portals.broadinstitute.org/ccle/data. Protein expression[43] data were directly exported from the
531 indicated reference.
532

533 GTEx data

534 GTEx v8 gene expression data (phs000424.v8) where processed as described above (RNA-seq pipeline
535 v2.0 (C-GET)[74]). For 4 samples processing failed, and 582 samples failed QC based on sequence length,
536 GC content, assigned reads, intronic bases, 3'/5' biases, uniquely mapped reads or *GAPDH* detection,
537 and were not included into the final object. Samples from the "Cells - Transformed fibroblast", "Cells -
538 EBV-transformed lymphocytes" and "Cells - Leukemia cell line (CML)" classes are omitted from the data
539 set.
540

541 CRISPR/Cas9 depletion assays

542 All CRISPR/Cas9 depletion assays were conducted as previously described[80]. In brief, gRNA sequences
543 were cloned into their respective vector backbone, typically containing GFP (Supplementary Table 4), at
544 Genscript Biotech Corporation. Lentiviral particles were produced in 293T-Lenti-X (Clontech) cells
545 cultured in DMEM, 10% Tet-system approved FCS, 1X Glutamax, 1X NaPyr. 4 x 10^6 cells were plated in 8
546 ml medium in 10 cm dishes and transiently transfected with 7 µg of plasmid DNA mixed with Lenti-X
547 Packaging Single Shots (VSV-G) (TakaraBio) according to the manufacturer's instructions on the following
548 day. 4 hours after transfection, 6 ml fresh medium was added to the plates. Supernatant was harvested
549 48 hours after transfection, filtered through a 0.45 µm PVDF filter (Millipore) and stored at -80°C in
550 unconcentrated aliquots until further use. Relevant cell lines stably expressing Cas9 (see Supplementary
551 Table 4) were plated at approximately 50 –60 % confluence in 12 or 24 well plates and transduced with
552 250-500 µl of gRNA virus to achieve 10%-95% transduction efficiency. After transduction, the fraction of
553 GFP positive cells was determined at indicated timepoints using flow cytometry.
554 Where cell lines expressing doxycycline-inducible cDNA constructs were included in depletion assays,
555 expression was induced at the start of the experiment by addition of 0.5-1 µg/ml doxycycline to the
556 medium, which was thereafter replenished twice per week.
557

558 siRNA assay
559 Cells were seeded at a density of 4 x 10^5 in 6-well plates in standard culture media. 24 hours after
560 seeding, cells were transfected with OTP Smartpool reagents (Horizon Discovery) targeting *CSTF2*
561 individually or in an equimolar mixture, *CSTF2T* or negative control at a final concentration of 20 nM
562 using RNAiMAX (Invitrogen) as specified by the manufacturer. 24 hours post transfection media was
563 exchanged and cells further incubated for 48 hours. siRNA details are listed in Supplementary Table 4.
564

565 cDNA overexpression

566 Constructs based on the pMSCV-Linker-PGK-Blasti backbone (see Supplementary Table 4) were
567 packaged into viral particles using the Platinum-GP Retrovial Packaging Cell line (). Briefly, 5 x 10^6 cells
568 were plated in 10 cm dishes and co-transfected with 3 µg VSV-G plasmid and 9 µg of the respective
569 construct Lipofectamine LTX (Thermo Fisher) the following day. Medium was exchanged after 16 h and
570 harvested 48 h later for filtration using 0.45 µm PVDF filter (Millipore) and subsequent storage at –80 °C
571 before transduction of target cells and subsequent selection of successfully transduced cells through
572 addition of Blasticidin to the medium.

573 Constructs based on the RT3REN backbone (see Supplementary Table 4) were packaged into lentiviral
574 particles using the Platinum-E packaging cell line (Cell Biolabs). In brief, 600,000 cells were plated in 6

575 well plates and transfected with 2 µg plasmid DNA using 6 µl Lipofectamine LTX reagent (Thermo
576 Fisher). Medium was exchanged after 16 h and harvested 24 h later, filtered through a 0.45 µm PVDF
577 filter (Millipore) and added directly to recipient cells stably expressing an ecotropic receptor (pRRL-
578 RIEH), followed by selection with Geneticin. Lentivirus for pRRL-RIEH was produced in lenti X 293T-Lenti-
579 X (Clontech). 4 x 10^6 cells were plated in 8 ml medium in 10 cm dishes and transiently transfected with 7
580 µg of plasmid DNA mixed with Lenti-X Packaging Single Shots (VSV-G) (TakaraBio) according to the
581 manufacturer's instructions on the following day. 4 hours after transfection, 6 ml fresh medium was
582 added to the plates. Supernatant was harvested 48 hours after transfection, filtered through a 0.45 µm
583 PVDF filter (Millipore) before addition to cells and subsequent selection with Hygromycin.

584

585 Western blot

586 Cells were lysed using RIPA buffer (Sigma) supplemented with HALT protease and phosphatase inhibitor
587 cocktail (Thermo Fisher). Lysates were incubated on ice for 30 min, centrifuged at 14,000 rcf for 20 min
588 at 4°C and protein amounts in the supernatant determined using the Bradford assay (BioRad) according
589 to the manufacturer's instructions. Laemmli buffer was added to samples followed by boiling at 95 °C for
590 5 min. Samples were loaded on a pre-cast gel (Criterion XT Precast 4-12 % Bis-Tris Gel, BioRad), run at
591 150 V for 1.5 hours in XT MOPS running buffer (BioRad) before transfer onto a nitrocellulose membrane
592 (Transblot Turbo Transfer Pack Midi 0.2 µm) for 7 min using the Transblot Turbo Transfer System
593 (BioRad, program: Quickblot Mixed MW, Midi Gel). Membranes were incubated for 1 hour in blocking
594 buffer (10% BSA, 10% PBS-T in water) followed by overnight incubation at 4 °C with primary antibody in
595 BSA antibody buffer (5 % BSA in PBS-T). The next day, membranes were washed three times with PBS-T
596 (10 min per wash) and incubated with secondary antibody in Casein antibody buffer (0,1% Casein in PBS-
597 T) for 1 hour in the dark at room temperature. Membranes were washed three times in PBS-T (10 min
598 per wash) and visualized on an Odyssey CLx imaging system (LI-COR Biosciences).

599 All antibody details can be found in Supplementary Table 4.
600

601 Correlation analysis (PaCT)

602 Depletion data for individual genes were obtained from three studies: DRIVE[42] (2017-10-01), AVANA[40]
603 (21Q1) and Sanger[41] (Release 1). Subsequently, depletion values for every screened gene with unique
604 gene symbols were correlated to expression values (TPM, see above), methylation[44] or protein
605 expression[43] data across the screened cell lines. Methylation data were summarized for genomic regions
606 mapping to a gene. Pearson, Spearman and Kendall correlation coefficients and corresponding p-values
607 were collected. The gene with depletion data is referred to as *query (q)* gene and the gene with
608 expression/methylation data is referred to as *biomarker (b)* for pairwise correlations. Subsequently, data
609 were filtered for genes which are part of a paralog family, such that every pairwise correlation between
610 *q* and *b* is considered if *q* and *b* are part of the same paralog family:

611 $$A = \{q, b \mid q \wedge b \in of\ same\ paralog\ family\}\ where\ A \subseteq B$$

612 where *B* denotes all correlations between *query* and *biomarker* pairs (screened genes (*q*) and genes with
613 protein and/or mRNA expression values(*b*)) and *A* denotes all correlations for a given paralog family.

614 We used Spearman coefficients and p-values for all subsequent analyses to account for possible non-
615 normal distributions in the data and minimize the impact of outlier values. Due to differences in query
616 and cell line libraries used, and different scoring systems, each sub-dataset that was processed
617 separately (AVANA, Sanger and DRIVE scores for gene and protein expression). For each sub-dataset, we
618 calculated its own cutoff at 3*SD (standard deviation) and additionally filtered for p-value < 0.05. For
619 gene expression data, all p-values at the 3*SD cutoff were highly significant, likely due to the more
620 complete source data for this domain.

621 The complete PaCT results can be found in Supplementary Table 2.
622

623 PaCT exploratory space

624 For all 3,587 paralog families with at least two members, we computed all possible pairwise interactions
625 across members of the same paralog family, including self-interactions. This approach resulted in a total
626 of 3,0841,147 potential pairs. We then assessed the potential of our approach to detect and quantify
627 pairwise dependencies by depletion-expression correlation. Pairs where the query gene was not
628 targeted in any depletion dataset and/or targeted in zero cell lines, and without gene expression data
629 for the biomarker gene expression were labeled as "no info both". Pairs for which information was
630 missing for either depletion or gene expression were labeled as "no info query" and "no info
631 biomarker", respectively. Pairs for which information was available in only a single cell line do not allow
632 calculation of a correlation and were labeled "1 cell line". Pairs for which information was available both
633 for the query and biomarker in at least two cell lines was labeled as "info query & biomarker". Protein
634 expression data were not included in this analysis.
635

636 PaCT simulation analysis

637 To identify the difference between PaCT hit correlations and random correlations, we performed 1000
638 simulations for each gene from each family with significant interactions. For each query gene *q* from each
639 family *f*, we generated a vector of genes *v* with same size as *f*. The new set of genes in *v* contains only the
640 query gene from *f* but the remaining genes in *v* are sampled without replacement from the remaining
641 paralogue families. Then pairwise correlations were computed as above.
642

643 Wilcoxon-test analysis

644 Cell lines were split into sensitive, resistant and intermediate groups using a k-means clustering
645 algorithm with k=3 for the depletion scores of every gene in the DRIVE[42], AVANA[40] and Sanger[41]
646 datasets. For cell lines in the sensitive and resistant bins, gene and protein expression data were
647 collected. Subsequently, a non-parametric test (Wilcoxon test) was conducted for all query-biomarker
648 pairs. p-values were collected and corrected for multiple testing (Benjamini-Hochberg). The query-
649 biomarker pairs were then filtered as described above.
650

651 Random Forest model

652 CCLE gene expression data of chrY-encoded and *DDX3X, EIF1AX, ZFX* and *RPS4X* paralog family genes
653 were used to train a Random Forest (RF) model on the Sanger[41] depletion data. k-means clustering (as

654 described above) was used to separate sensitive and insensitive cell lines. Subsequently, AVANA[40]
655 sensitivity data were predicted using the RF model.
656

657 Ortholog analysis

658 We first converted our list of human paralogs to the best match ortholog in *M. musculus*, *D.*
659 *melanogaster*, *D. rerio*, *C. elegans* or *S. cerevisiae* using DIOPT[81] (v8). Then we added information on
660 each gene's essentiality from OGEE[82] (v2), with a majority vote decision on calling a gene essential or
661 non-essential in cases where more than one dataset with ambiguous calls existed. For all paralog
662 interaction hit pairs, we then checked whether query and biomarker share the same ortholog gene and
663 if so, whether the ortholog is essential.
664

665 Multi-mapping gRNA analysis

666 We downloaded information on dropped gRNAs and gRNA mapping for the AVANA library from
667 https://depmap.org/portal/download/. Based on this information, we extracted the number of
668 dropped, uniquely mapped or multi-mapping gRNAs for each query gene in the list of PaCT pairs.

669

670 LOY inference

671 In addition to gene expression and copy number (CN) data, TCGA, GTEx and CCLE provide annotation of
672 the sex of the patients where a sample/cell line originated from. We calculated (i) the average TPM, (ii)
673 the maximum TPM, (iii) the average raw count, (iv) the average relative CN, and (v) the average absolute
674 CN for all genes located on chrY for all samples. TCGA and GTEx do not provide CN data for chrY. For
675 samples originally annotated as male, we checked whether *all* of their values (i)-(v) for cell lines and (i)-
676 (iii) for tissue samples were below the respective 99th percentile of female samples. If this was the case,
677 we re-annotated the sample as LOY.
678

679 PCR validation of LOY

680 Genotyping primer pairs for different genes on chrX and chrY were designed and tested for specificity.
681 Genomic DNA was extracted from female, male and LOY cells using the QIAamp DNA Mini Kit (Qiagen)
682 following the manufacturer's protocol. PCR was run using AmpliTaqGold DNA polymerase (Thermo
683 Fisher Scientific) with 100 ng genomic DNA as input. 55°C annealing temperature was used for all primer
684 pairs. Resulting amplicons analyzed on a 2% agarose gel. All primer sequences are listed in
685 Supplementary Table 4.
686

687 Induction of LOY

688 One million HT-1080 cells expressing Cas9 (puromycin) and *DDX3X* (blasticidin) or *ZFX* (blasticidin)
689 constructs were transiently transfected with a pool of 18 GFP-containing plasmids encoding for gRNAs
690 targeting different chrY genes (RN-gRNA_429-434, RN-gRNA_441-443, RN-gRNA_458-466 using
691 Lipofectamine 3000 (Thermo Fisher Scientific) according to the manufacturer's instructions. 48 hours

692 after transfection, GFP-positive cells were isolated by FACS and diluted to obtain single cell clones.
693 Clones were screened for LOY by PCR from genomic DNA (as described above) using standard laboratory
694 techniques. Clones with PCR products for chrX but without PCR products for chrY were selected. gRNA
695 sequences are listed in Supplementary Table 4.
696

697 Software and data availability

698 All calculations were performed in R. Data were visualized using R or GraphPad Prism. All data are
699 publicly available through the indicated references and provided as Supplementary Material, including
700 an R Markdown script containing all code and versioning information to reproduce analyses and figures.

701

702 **Acknowledgements**

703 We wish to thank Norbert Schweifer, Tamara Tröls, Harald Studensky and Silvia Blaha-Ostermann for
704 technical assistance, Johannes Zuber for help with cloning the paralog gRNA library, and all colleagues at
705 Boehringer Ingelheim RCV Cancer Research Target Discovery for discussions and critical input to the
706 manuscript.

707

708 **Conflict of Interest**

709 Authors are full time employees of Boehringer Ingelheim.

710

711 **Author Contributions**

712 A.K., A.H., F.S., T.P., S.O., C.W., M.C., and C.R. conducted wet lab experiments. A.K., A.S., A.P., V.T., F.S.,
713 B.M. and R.A.N. conducted bioinformatic analyses. R.A.N. and B.M. conceived study. B.M., R.A.N. and
714 M.P. oversaw study. J.P., S.W., A.S., led paralog library screens. A.S. helped conceptualize study. A.K.,
715 B.M. and R.A.N. wrote manuscript with input from all other

716

717 **Figures and Figure Legends**

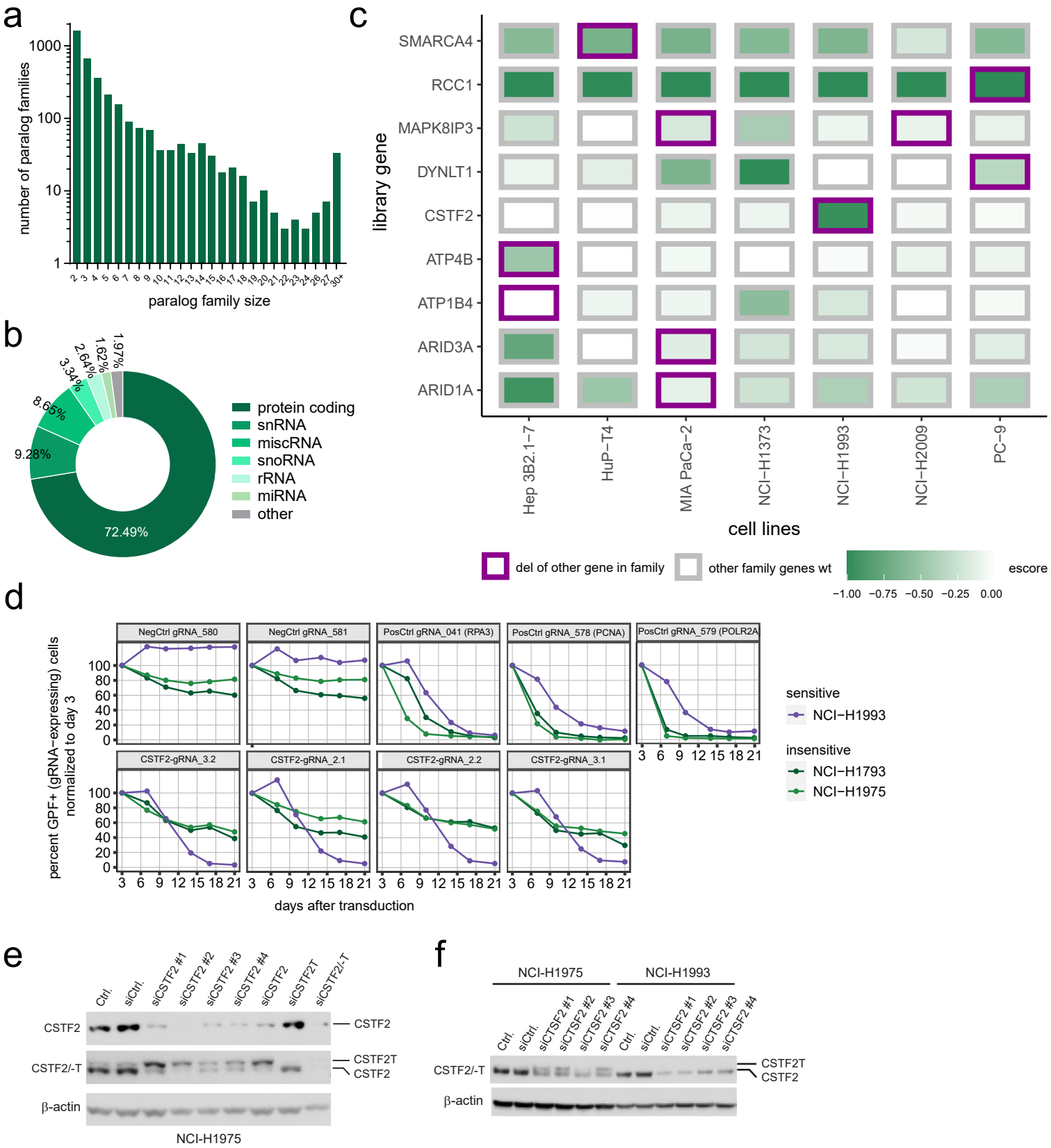
a
number of paralog families
paralog family size
b
protein coding
snRNA
miscRNA
snoRNA
rRNA
miRNA
other
72.49%
9.28%
8.65%
3.34%
2.64%
1.62%
1.97%
c
library gene
SMARCA4
RCC1
MAPK8IP3
DYNLT1
CSTF2
ATP4B
ATP1B4
ARID3A
ARID1A
Hep 3B2.1−7
HuP−T4
MIA PaCa−2
NCI−H1373
NCI−H1993
NCI−H2009
PC−9
cell lines
del of other gene in family
other family genes wt
escore
−1.00 −0.75 −0.50 −0.25 0.00
d
NegCtrl gRNA_580
NegCtrl gRNA_581
PosCtrl gRNA_041 (RPA3)
PosCtrl gRNA_578 (PCNA)
PosCtrl gRNA_579 (POLR2A)
CSTF2-gRNA_3.2
CSTF2-gRNA_2.1
CSTF2-gRNA_2.2
CSTF2-gRNA_3.1
percent GPF+ (gRNA−expressing) cells normalized to day 3
days after transduction
sensitive
NCI−H1993
insensitive
NCI−H1793
NCI−H1975
e
Ctrl.
siCtrl.
siCSTF2 #1
siCSTF2 #2
siCSTF2 #3
siCSTF2 #4
siCSTF2
siCSTF2T
siCSTF2/-T
CSTF2
CSTF2/-T
β-actin
CSTF2T
NCI-H1975
f
NCI-H1975
NCI-H1993

Figure 1

718 Figure 1: Proof-of-concept paralog dependency CRISPR screens reveal a functional interaction of *CSTF2*
719 and *CSTF2T*.

720 a-b) Distribution of paralog families in study by family size (a) and gene type (b).
721 c) CRISPR screen results in 7 cancer cell lines. Only genes with escore < -0.4 and FDR < 0.1 are
722 displayed. Shades of green indicate effect size (escore), box color indicates whether paralog
723 family contains deleted gene different from listed gene (del) or not (wt).
724 d) CRISPR/Cas9 depletion assay in cell lines resistant (green) and sensitive (purple) to loss of *CSTF2.*
725 gRNAs targeting positive control genes (*RPA3*, *POLR2A*, *PCNA*), negative controls (*NegCon03/-07*),
726 and *CSTF2* are indicated. Cells were lentivirally transduced with the gRNA plasmid containing GFP;
727 GFP percentage in transduced cell line pool was measured by flow cytometry at the indicated time
728 points and normalized to day 3 post-transduction.
729 e-f) Western blots for *CSTF2* and *CSTF2T* in lysates from indicated cell lines after siRNA treatment
730 (3d). β-actin was used as loading control.
731

732

Figure 2

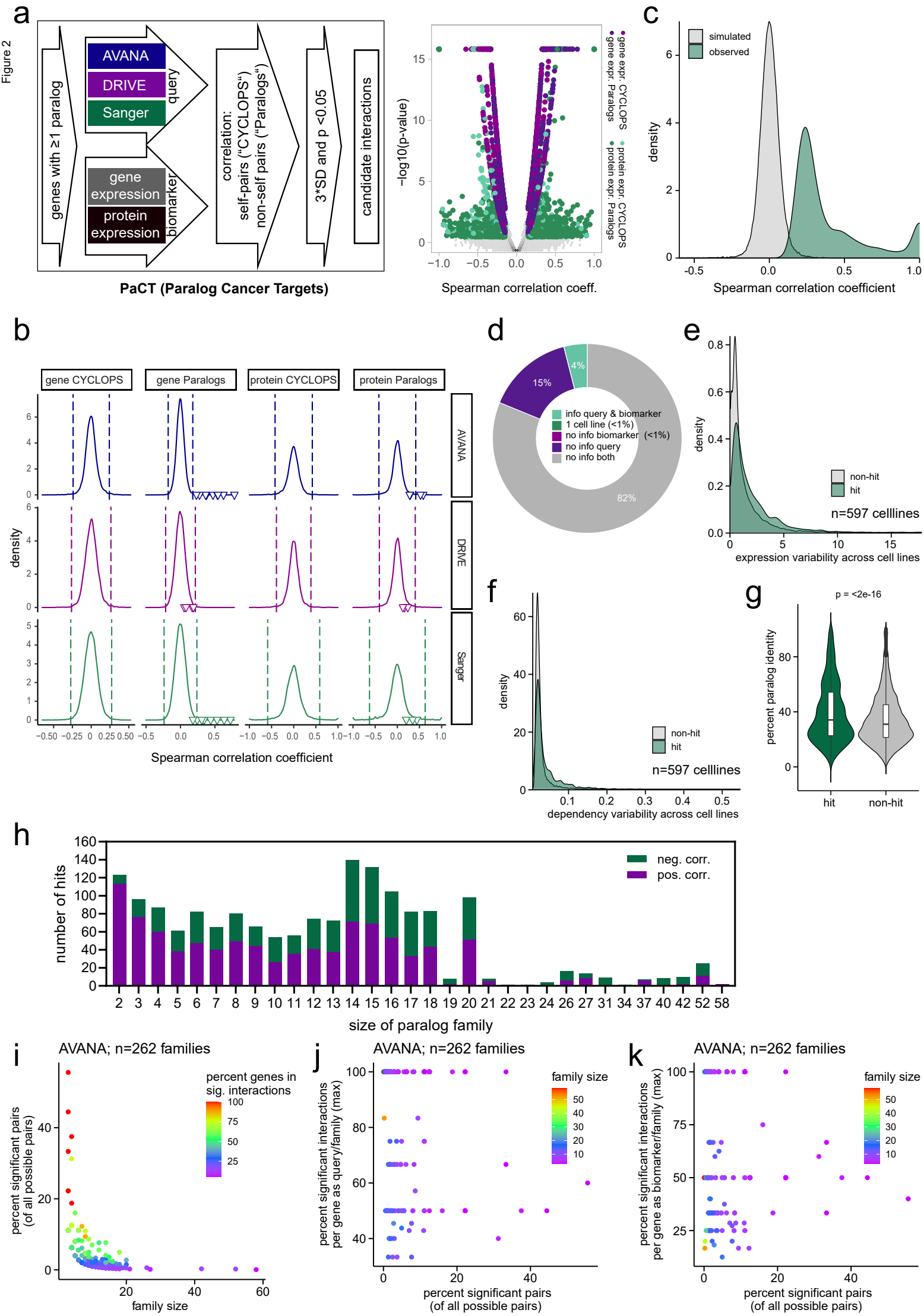
a
genes with ≥1 paralog
AVANA
DRIVE
Sanger
query
gene expression
protein expression
biomarker
correlation:
self-pairs ("CYCLOPS")
non-self pairs ("Paralogs")
3*SD and p <0.05
candidate interactions
PaCT (Paralog Cancer Targets)
−log10(p-value)
Spearman correlation coeff.
gene expr. CYCLOPS
gene expr. Paralogs
protein expr. CYCLOPS
protein expr. Paralogs
c
simulated
observed
density
Spearman correlation coefficient
b
gene CYCLOPS
gene Paralogs
protein CYCLOPS
protein Paralogs
AVANA
DRIVE
Sanger
density
Spearman correlation coefficient
d
4%
15%
82%
info query & biomarker
1 cell line (<1%)
no info biomarker (<1%)
no info query
no info both
e
density
non-hit
hit
n=597 celllines
expression variability across cell lines
f
density
non-hit
hit
n=597 celllines
dependency variability across cell lines
g
p = <2e-16
percent paralog identity
hit
non-hit
h
number of hits
neg. corr.
pos. corr.
size of paralog family
i
AVANA; n=262 families
percent genes in sig. interactions
percent significant pairs (of all possible pairs)
family size
j
AVANA; n=262 families
family size
percent significant interactions per gene as query/family (max)
percent significant pairs (of all possible pairs)
k
AVANA; n=262 families
family size
percent significant interactions per gene as biomarker/family (max)
percent significant pairs (of all possible pairs)

733 Figure 2: Correlation analysis of public loss-of-function screens yield to identify paralog genetic
734 interactions.

735 a) PaCT analysis workflow and volcano plot of tested pairs by dataset (CYCLOPS, self-interactions;
736 Paralogs, pairwise paralog interactions within same family). See Methods for details.
737 b) Distribution of PaCT correlations (Spearman) by input datasets. Triangles indicate specific hit
738 pairs mentioned in subsequent analyses. Dashed lines mark the 3-standard-deviations cutoff
739 used for hit filtering.
740 c) Distribution of Spearman correlation coefficients of randomly assigned genes to each query
741 compared to the correlation distribution of original PaCT hits.
742 d) Pie chart displaying different categories of query-biomarker pairs across the complete
743 theoretical PaCT exploratory space. Only pairs for which information for both query and
744 biomarker is available can yield hit interactions. See Methods for details.

745 e, f) Expression (e) and depletion score (f) variability distribution of genes involved in hit and non-hit
746 interactions across cell lines.

747 g) Nucleotide sequence similarity difference between hit and non-hit pairs.
748 h) Number of unique hit pairs in paralog families of different size, grouped by type of correlation.
749 i) Percentage of hit pairs identified in each family plotted against family size. Color legend
750 indicates the percentage of genes of the respective family involved in hit interactions, either as
751 query or biomarker.

752 j, k) Percentage of hit interactions per gene as a query (j) and as a biomarker (k) is plotted against
753 percentage of hit interactions per family. Color indicates family size.
754

755

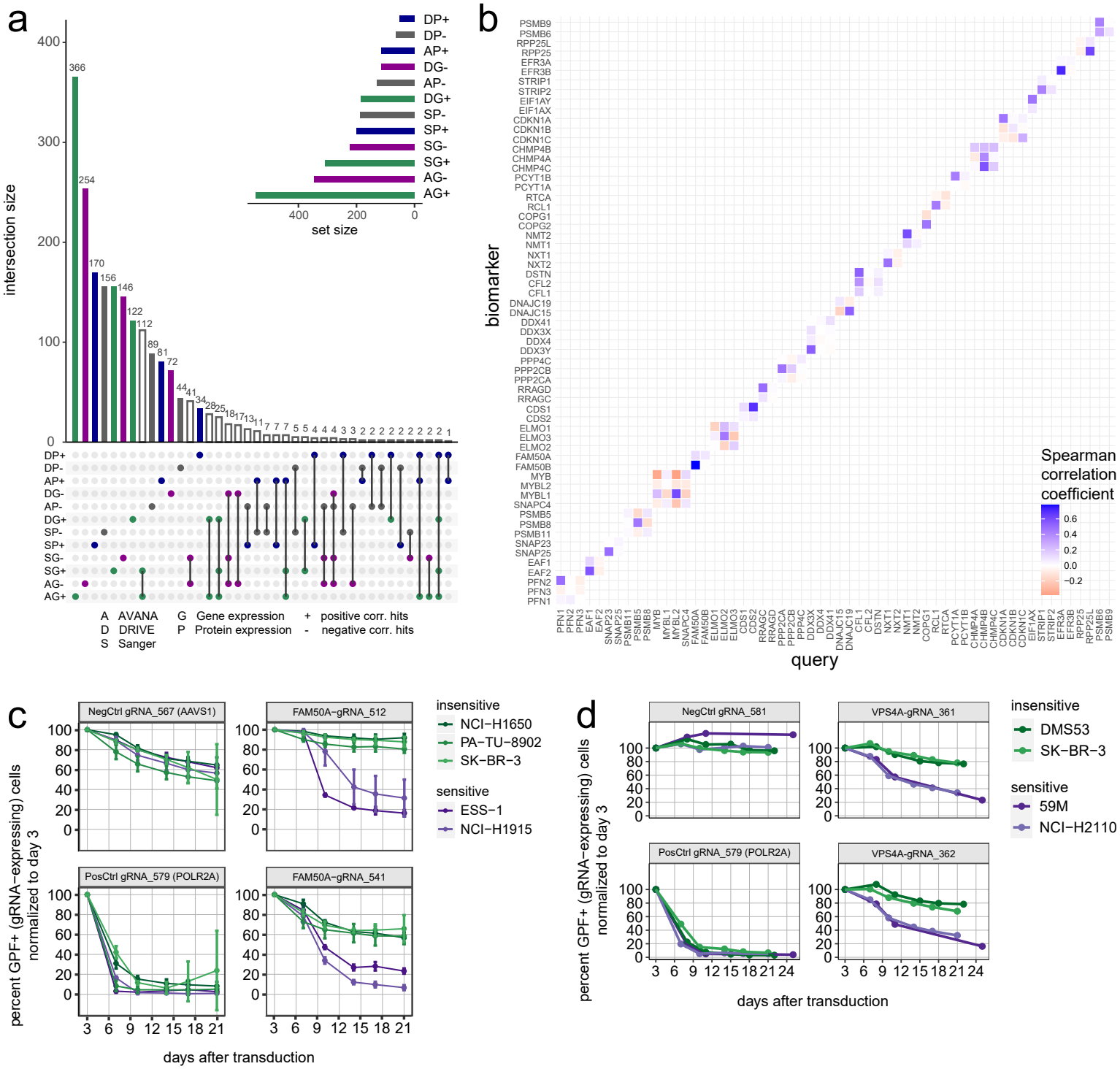
a
intersection size
set size
DP+
DP-
AP+
DG-
AP-
DG+
SP-
SP+
SG-
SG+
AG-
AG+
A AVANA
D DRIVE
S Sanger
G Gene expression
P Protein expression
+ positive corr. hits
- negative corr. hits
b
biomarker
query
Spearman correlation coefficient
c
NegCtrl gRNA_567 (AAVS1)
FAM50A-gRNA_512
PosCtrl gRNA_579 (POLR2A)
FAM50A-gRNA_541
percent GPF+ (gRNA-expressing) cells normalized to day 3
days after transduction
insensitive
NCI-H1650
PA-TU-8902
SK-BR-3
sensitive
ESS-1
NCI-H1915
d
NegCtrl gRNA_581
VPS4A-gRNA_361
PosCtrl gRNA_579 (POLR2A)
VPS4A-gRNA_362
percent GPF+ (gRNA-expressing) cells normalized to day 3
days after transduction
insensitive
DMS53
SK-BR-3
sensitive
59M
NCI-H2110

Figure 3

756 Figure 3: Correlation analysis of public loss-of-function screens yield known and novel candidate paralog
757 genetic interactions.

758 a) Overlap of hit pairs between different input datasets. Y-axis shows the number of overlapping
759 pairs by dataset. Comparisons are indicated by dots and lines on the x-axis, colored by type of
760 expression data (gene, protein) and interaction (pos, neg). Inset shows number of hit pairs by
761 dataset.
762 b) Exemplary pairwise correlation matrix for paralog families of 2-4 members and Spearman
763 correlation > 0.42 for at least one pair in the family including CYCLOPS interactions.
764 c) CRISPR/Cas9 depletion assay in cell lines resistant (green) and sensitive (purple) to loss of
765 *FAM50A.* gRNAs targeting positive control genes (*POLR2A*), negative controls (*AAVS1*) and
766 *FAM50A* are indicated. Cells were lentivirally transduced with the gRNA plasmid containing GFP;
767 GFP percentage in the transduced cell line pool was measured by flow cytometry at the
768 indicated time points and normalized to day 3 post-transduction.
769 d) CRISPR/Cas9 depletion assay in cell lines resistant (green) and sensitive (purple) to loss of
770 VPS4*A.* gRNAs targeting positive control genes (*POLR2A*), negative controls (*non-targeting*) and
771 *VPS4A* are indicated. Cells were lentivirally transduced with the gRNA plasmid containing GFP;
772 GFP percentage in the transduced cell line pool was measured by flow cytometry at the
773 indicated time points and normalized to day 3 post-transduction.
774

775

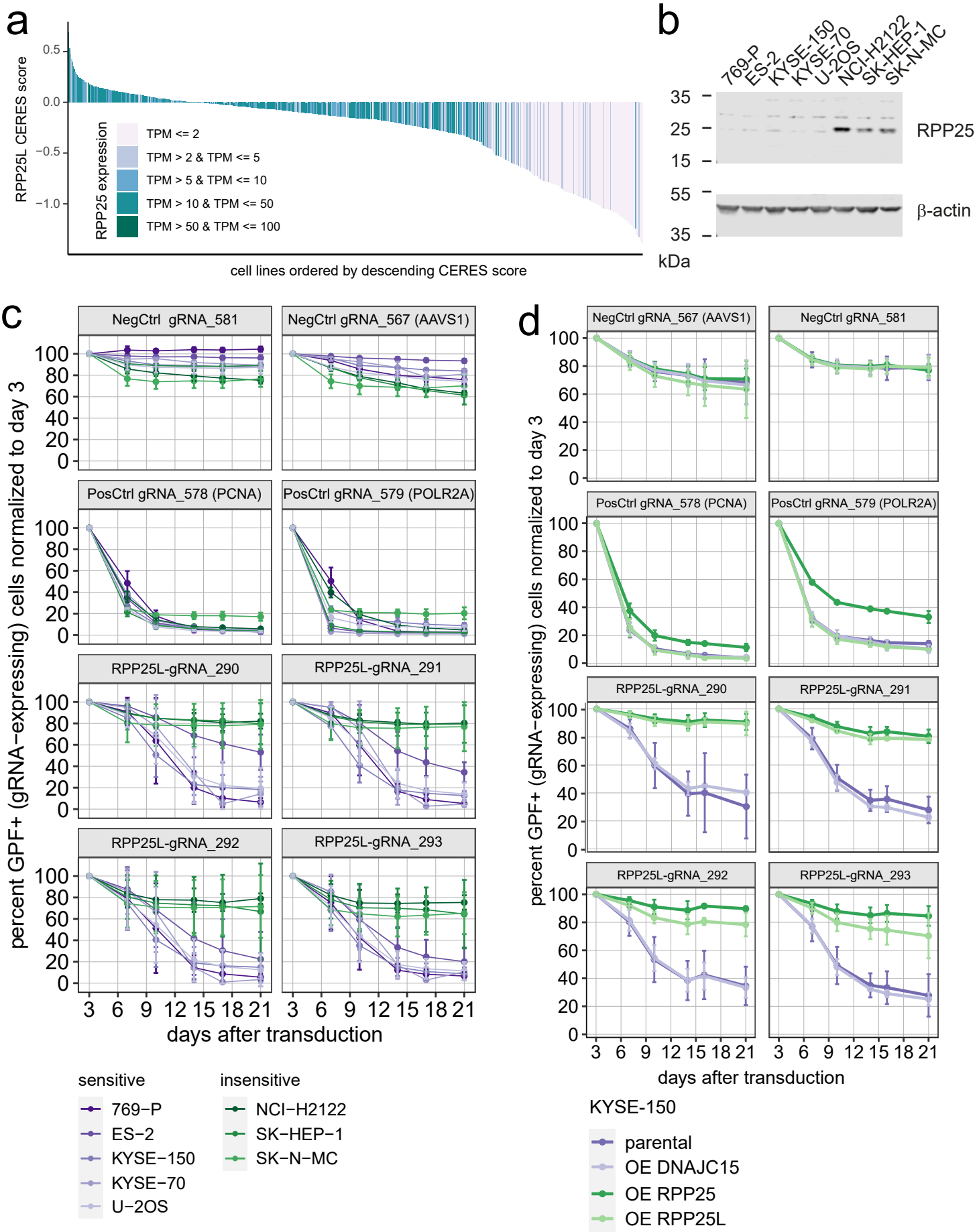
a
RPP25L CERES score
0.5
0.0
−0.5
−1.0
RPP25 expression
TPM <= 2
TPM > 2 & TPM <= 5
TPM > 5 & TPM <= 10
TPM > 10 & TPM <= 50
TPM > 50 & TPM <= 100
cell lines ordered by descending CERES score
b
769-P
ES-2
KYSE-150
KYSE-70
U-2OS
NCI-H2122
SK-HEP-1
SK-N-MC
35
25
15
55
35
kDa
RPP25
β-actin
c
NegCtrl gRNA_581
NegCtrl gRNA_567 (AAVS1)
PosCtrl gRNA_578 (PCNA)
PosCtrl gRNA_579 (POLR2A)
RPP25L-gRNA_290
RPP25L-gRNA_291
RPP25L-gRNA_292
RPP25L-gRNA_293
percent GPF+ (gRNA−expressing) cells normalized to day 3
days after transduction
sensitive
769−P
ES−2
KYSE−150
KYSE−70
U−2OS
insensitive
NCI−H2122
SK−HEP−1
SK−N−MC
d
NegCtrl gRNA_567 (AAVS1)
NegCtrl gRNA_581
PosCtrl gRNA_578 (PCNA)
PosCtrl gRNA_579 (POLR2A)
RPP25L-gRNA_290
RPP25L-gRNA_291
RPP25L-gRNA_292
RPP25L-gRNA_293
percent GPF+ (gRNA−expressing) cells normalized to day 3
days after transduction
KYSE-150
parental
OE DNAJC15
OE RPP25
OE RPP25L

Figure 4

776 Figure 4: Validation of paralog redundancy between *RPP25* and *RPP25L*.

777 a) AVANA-based depletion scores (CERES) for *RPP25L,* color-coded by *RPP25* expression levels.
778 b) Western blot for *RPP25* in indicated cancer cell lines. β-actin was used as loading control.
779 c) CRISPR/Cas9 depletion assay in cell lines predicted to be sensitive (purple) or resistant (green) to
780 loss of *RPP25L*. gRNAs targeting *RPP25L* (gRNA-290, gRNA-291, gRNA-292, gRNA-293), positive
781 controls (*PCNA*, *POLR2A*) and negative controls (non-targeting, *AAVS1*) are indicated. Cells were
782 lentivirally transduced with the gRNA plasmid containing GFP; GFP percentage in transduced cell
783 line pool was measured by flow cytometry at the indicated time points and normalized to day 3
784 post-transduction (n=3 independent replicates of the experiment).
785 d) CRISPR/Cas9 depletion assay as in (c) following ectopic expression of *RPP25* or *RPP25L* in KYSE-
786 150 cells that are sensitive to loss of *RPP25L* (parental). *DNAJC15* expression served as a
787 negative control.
788

789

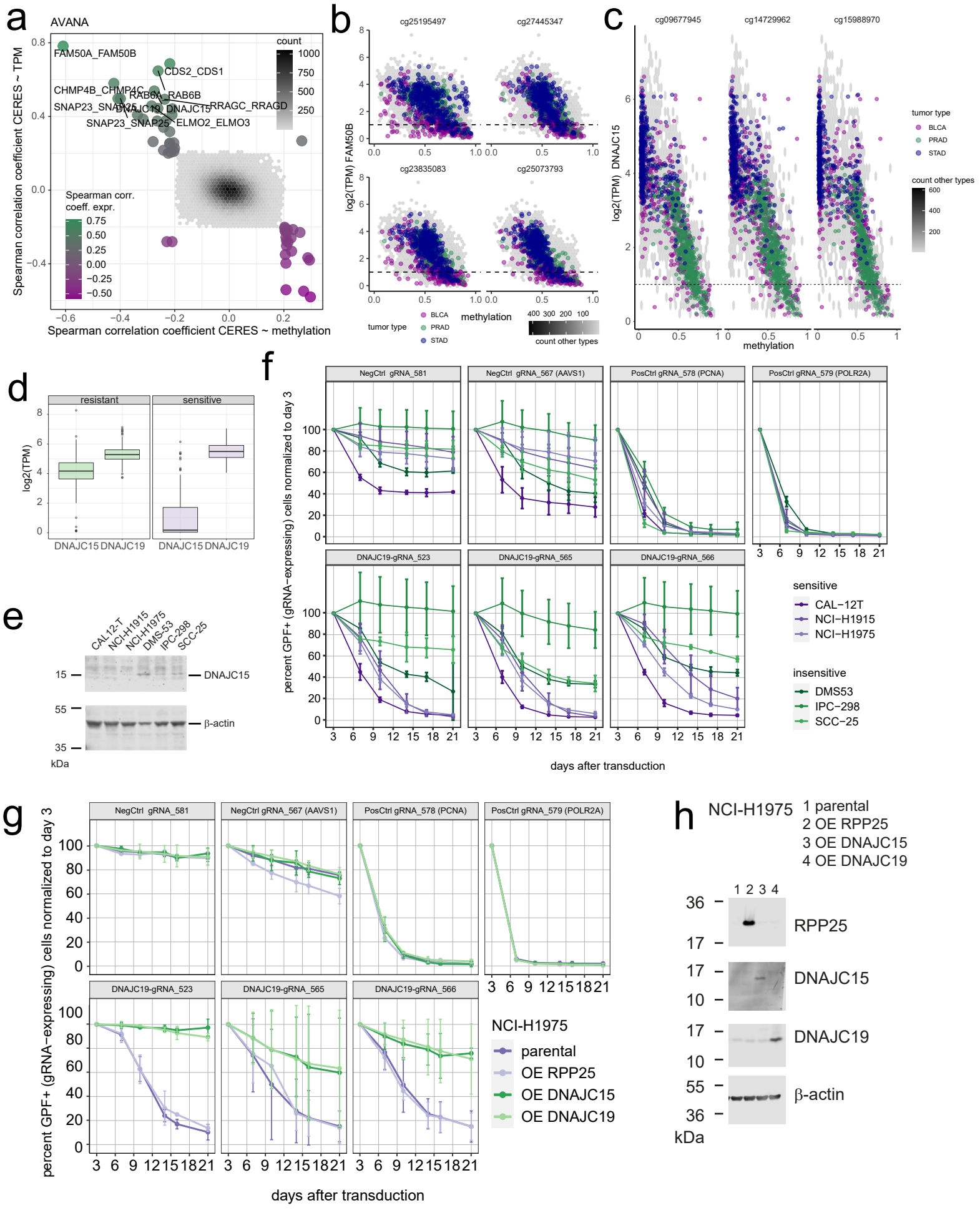
a
AVANA
FAM50A_FAM50B
CDS2_CDS1
CHMP4B_CHMP4C
RAB6A_RAB6B
SNAP23_SNAP25
DNAJC19_DNAJC15
RRAGC_RRAGD
SNAP23_SNAP25_ELMO2_ELMO3
count
Spearman corr. coeff. expr.
Spearman correlation coefficient CERES ~ TPM
Spearman correlation coefficient CERES ~ methylation
b
cg25195497
cg27445347
cg23835083
cg25073793
log2(TPM) FAM50B
methylation
tumor type
BLCA
PRAD
STAD
count other types
c
cg09677945
cg14729962
cg15988970
log2(TPM) DNAJC15
methylation
tumor type
count other types
d
resistant
sensitive
log2(TPM)
DNAJC15 DNAJC19 DNAJC15 DNAJC19
e
CAL-12-T
NCI-H1915
NCI-H1975
DMS-53
IPC-298
SCC-25
DNAJC15
β-actin
kDa
f
NegCtrl gRNA_581
NegCtrl gRNA_567 (AAVS1)
PosCtrl gRNA_578 (PCNA)
PosCtrl gRNA_579 (POLR2A)
DNAJC19-gRNA_523
DNAJC19-gRNA_565
DNAJC19-gRNA_566
percent GPF+ (gRNA−expressing) cells normalized to day 3
days after transduction
sensitive
CAL−12T
NCI−H1915
NCI−H1975
insensitive
DMS53
IPC−298
SCC−25
g
NegCtrl gRNA_581
NegCtrl gRNA_567 (AAVS1)
PosCtrl gRNA_578 (PCNA)
PosCtrl gRNA_579 (POLR2A)
DNAJC19-gRNA_523
DNAJC19-gRNA_565
DNAJC19-gRNA_566
percent GPF+ (gRNA−expressing) cells normalized to day 3
days after transduction
NCI-H1975
parental
OE RPP25
OE DNAJC15
OE DNAJC19
h
NCI-H1975
1 parental
2 OE RPP25
3 OE DNAJC15
4 OE DNAJC19
1 2 3 4
RPP25
DNAJC15
DNAJC19
β-actin
kDa

Figure 5

790 Figure 5: Paralog redundancies for *FAM50A-FAM50B* and *DNAJC15-DNAJC19* can be attributed to
791 expression loss by DNA methylation.

792 a) Scatter plot identifying putative paralog dependencies due to DNA hypermethylation. X-axis:
793 Spearman correlation coefficient between depletion data (CERES score (AVANA data)) and DNA
794 methylation. Y-axis: Spearman correlation coefficient between depletion data (CERES score
795 (AVANA data)) and gene expression (TPM). Pairs with correlation coefficients <|0.2| are
796 displayed as density plots, strongest correlations are labeled.
797 b) Scatter plot of mRNA expression levels (log2(TPM)) of *FAM50B* versus CpG island methylation at
798 indicated loci across tumour types from TCGA. Samples from bladder urothelial carcinoma
799 (BLCA), prostate adenocarcinoma (PRAD) and stomach adenocarcinoma (STAD) studies are
800 highlighted.
801 c) Scatter plot of mRNA expression levels (log2(TPM)) of *DNAJC15* versus CpG island methylation at
802 indicated loci across tumour types from TCGA. Samples from bladder urothelial carcinoma
803 (BLCA), prostate adenocarcinoma (PRAD) and stomach adenocarcinoma (STAD) studies are
804 highlighted.
805 d) Boxplot summarizing expression data (log2(TPM)) for members of the *DNAJC19-DNAJC15*
806 paralog family in cell lines resistant and sensitive to *DNAJC19* loss.
807 e) Western blot of *DNAJC15* levels in selected sensitive (CAL-12T, NCI-H1915, NCI-H1975) and
808 resistant (DMS53, IPC-298, SCC-25) cell lines. β-actin was included as a loading control.
809 f) CRISPR/Cas9 depletion assay in cell lines predicted to be sensitive (purple) or resistant (green) to
810 loss of *DNAJC19*. gRNAs targeting *DNAJC19* (gRNA-318, gRNA-523, gRNA-565, gRNA-566),
811 positive controls (*PCNA*, *POLR2A*) and negative controls (non-targeting, *AAVS1*) are indicated.
812 Cells were lentivirally transduced with the gRNA plasmids also containing a GFP expression
813 cassette. The percentage of GFP expressing cells in the transduced cell line pool was measured
814 by flow cytometry at the indicated time points and normalized to day 3 post-transduction (n=3
815 independent replicates of the experiment).
816 g) CRISPR/Cas9 depletion assay in cell lines following ectopic expression of *DNAJC15* in NCI-H1975
817 cells that are sensitive to loss of *DNAJC19*. Expression was induced by addition of 1 µg/ml
818 doxycycline to the medium at the start of the experiment, which was replenished twice per
819 week. Cells were lentivirally transduced with a gRNA targeting *DNAJC19* (gRNA-318), positive
820 control (*POLR2A*) or negative control (non-targeting). The plasmid also expresses GFP. The
821 percentage of GFP-positive cells in transduced cell line pool was measured by flow cytometry at
822 the indicated time points and normalized to day 3 post-transduction (n=2 independent
823 replicates of the experiment).
824 h) Western blot for RPP25, DNAJC15, and DNAJC19 in NCI-H1975 cells expressing the indicated
825 overexpression constructs upon culture in the presence of doxycycline (1 µg/ml) for 72 hours. β-
826 actin was included as a loading control.
827

828

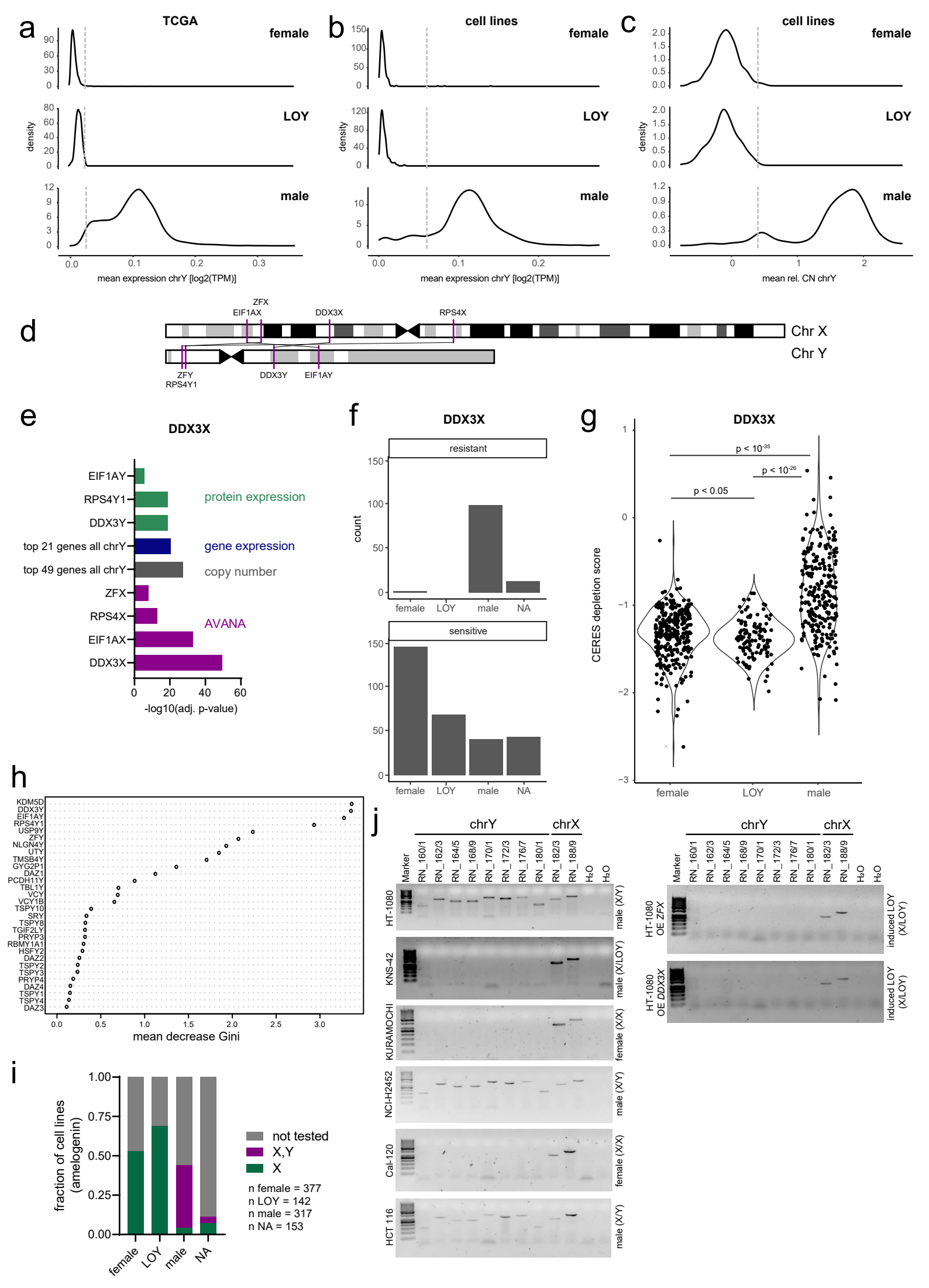
a
TCGA
female
LOY
male
density
mean expression chrY [log2(TPM)]
b
cell lines
female
LOY
male
density
mean expression chrY [log2(TPM)]
c
cell lines
female
LOY
male
density
mean rel. CN chrY
d
ZFX
EIF1AX
DDX3X
RPS4X
Chr X
Chr Y
ZFY
RPS4Y1
DDX3Y
EIF1AY
e
DDX3X
EIF1AY
RPS4Y1
DDX3Y
top 21 genes all chrY
top 49 genes all chrY
ZFX
RPS4X
EIF1AX
DDX3X
protein expression
gene expression
copy number
AVANA
-log10(adj. p-value)
f
DDX3X
resistant
sensitive
count
female
LOY
male
NA
g
DDX3X
p < 10^-35
p < 10^-26
p < 0.05
CERES depletion score
female
LOY
male
h
KDM5D
DDX3Y
EIF1AY
RPS4Y1
USP9Y
ZFY
NLGN4Y
UTY
TMSB4Y
GYG2P1
DAZ1
PCDH11Y
TBL1Y
VCY
VCY1B
TSPY10
SRY
TSPY8
TGIF2LY
PRYP3
RBMY1A1
HSFY2
DAZ2
TSPY2
TSPY3
PRYP4
DAZ4
TSPY1
TSPY4
DAZ3
mean decrease Gini
i
fraction of cell lines (amelogenin)
not tested
X,Y
X
n female = 377
n LOY = 142
n male = 317
n NA = 153
female
LOY
male
NA
j
chrY
chrX
Marker
RN_160/1
RN_162/3
RN_164/5
RN_168/9
RN_170/1
RN_172/3
RN_176/7
RN_180/1
RN_182/3
RN_188/9
H2O
H2O
HT-1080
KNS-42
KURAMOCHI
NCI-H2452
Cal-120
HCT 116
male (X/Y)
male (X/LOY)
female (X/X)
male (X/Y)
female (X/X)
male (X/Y)
HT-1080 OE ZFX
HT-1080 OE DDX3X
induced LOY (X/LOY)
induced LOY (X/LOY)

Figure 6

829 Figure 6: Loss of chrY as potential biomarker for paralog dependencies between sex chromosome genes.

830 a) Distribution of average gene expression (TPM) across genes located on chrY for TCGA samples
831 for which data were available. Sex (male, female) as annotated in TCGA or inferred (LOY) as
832 described in Methods.
833 b) As in (a) for cell lines (CCLE) with available gene expression data.
834 c) As in (b) for average relative copy number (CN).
835 d) Schematic depiction of chrX and chrY with location of interacting paralogs indicated.
836 e) Analysis of factors that are most significantly different between *DDX3X*-loss-sensitive and
837 *DDX3X*-loss-resistant cell lines, as defined using k-means clustering based on AVANA data. For
838 each data domain, the most significant discriminators are displayed.
839 f) Sensitive vs. resistant cell lines (as in (e)) by sex (as in (b and c)).
840 g) *DDX3X* sensitivity (CERES depletion score from AVANA dataset) by sex (as in (b and c)). p-values
841 were calculated using a two-sided Fisher's exact test for count data with Monte-Carlo-simulated
842 p-value (based on 10000 replicates).
843 h) Variable importance plot for Random Forest model to predict *DDX3X* sensitivity. Gene
844 expression values were used as variables for the Indicated genes on y-axis.
845 i) Fraction of cell lines that harbor chrX and chrY or chrX only, grouped by sex ((as in (b and c)), as
846 assessed by the amelogenin marker in standard STR analysis.
847 j) PCR validation of sex chromosome status in selected cell lines used for further analyses. 8 chrY-
848 specific primer pairs and 2 chrX-specific primer pairs were tested in female patient-derived
849 (KURAMOCHI and Cal-120), male patient-derived chrY retaining (HT-1080 and HCT 116), and
850 male LOY cells (KNS-42).
851

852

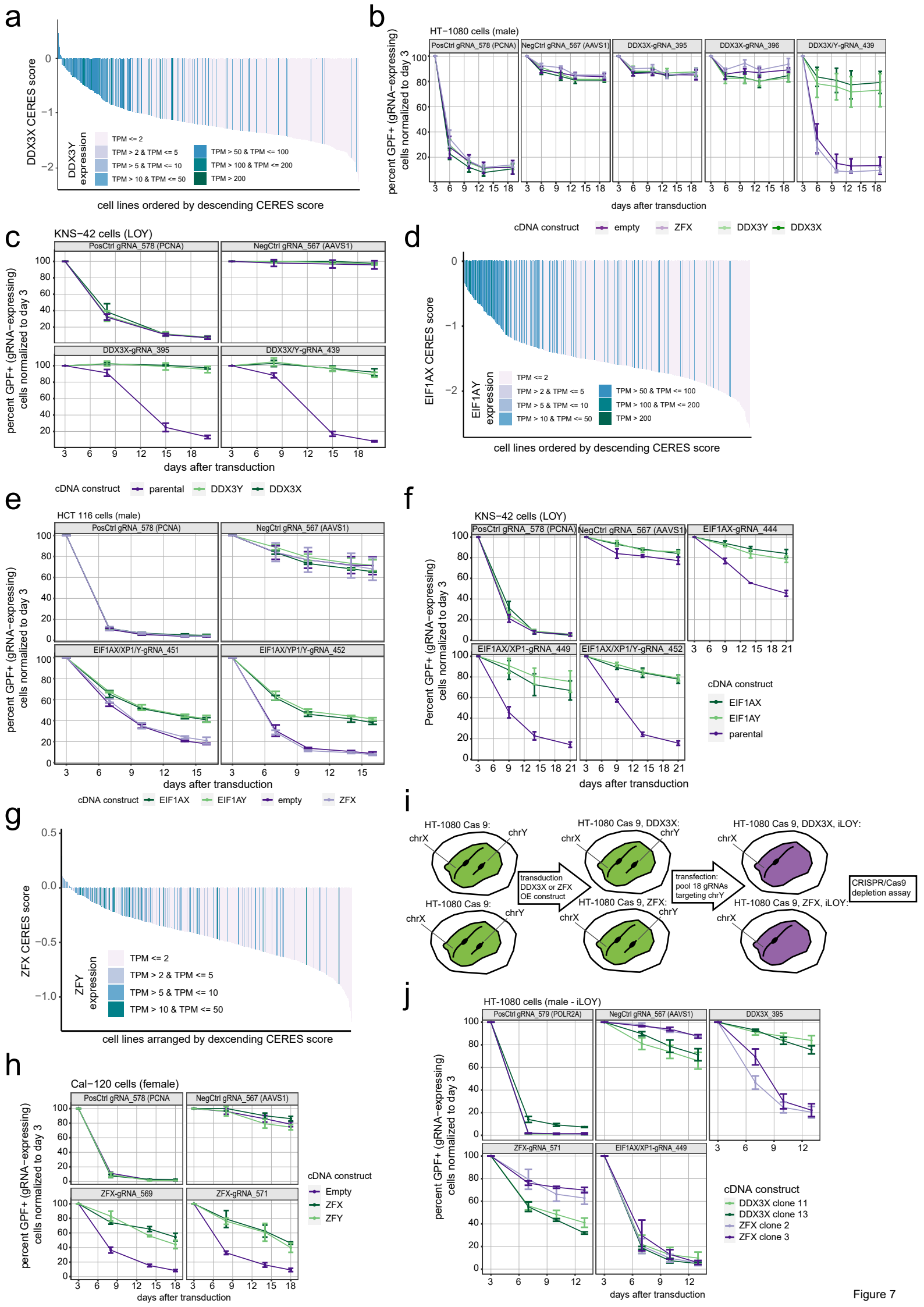
a
DDX3X CERES score
DDX3Y expression
TPM <= 2
TPM > 2 & TPM <= 5
TPM > 5 & TPM <= 10
TPM > 10 & TPM <= 50
TPM > 50 & TPM <= 100
TPM > 100 & TPM <= 200
TPM > 200
cell lines ordered by descending CERES score
b
HT−1080 cells (male)
PosCtrl gRNA_578 (PCNA)
NegCtrl gRNA_567 (AAVS1)
DDX3X-gRNA_395
DDX3X-gRNA_396
DDX3X/Y-gRNA_439
percent GPF+ (gRNA−expressing) cells normalized to day 3
days after transduction
cDNA construct
empty
ZFX
DDX3Y
DDX3X
c
KNS−42 cells (LOY)
PosCtrl gRNA_578 (PCNA)
NegCtrl gRNA_567 (AAVS1)
DDX3X-gRNA_395
DDX3X/Y-gRNA_439
percent GPF+ (gRNA−expressing) cells normalized to day 3
days after transduction
cDNA construct
parental
DDX3Y
DDX3X
d
EIF1AX CERES score
EIF1AY expression
TPM <= 2
TPM > 2 & TPM <= 5
TPM > 5 & TPM <= 10
TPM > 10 & TPM <= 50
TPM > 50 & TPM <= 100
TPM > 100 & TPM <= 200
TPM > 200
cell lines ordered by descending CERES score
e
HCT 116 cells (male)
PosCtrl gRNA_578 (PCNA)
NegCtrl gRNA_567 (AAVS1)
EIF1AX/XP1/Y-gRNA_451
EIF1AX/YP1/Y-gRNA_452
percent GPF+ (gRNA−expressing) cells normalized to day 3
days after transduction
cDNA construct
EIF1AX
EIF1AY
empty
ZFX
f
KNS−42 cells (LOY)
PosCtrl gRNA_578 (PCNA)
NegCtrl gRNA_567 (AAVS1)
EIF1AX-gRNA_444
EIF1AX/XP1-gRNA_449
EIF1AX/XP1/Y-gRNA_452
Percent GPF+ (gRNA−expressing) cells normalized to day 3
days after transduction
cDNA construct
EIF1AX
EIF1AY
parental
g
ZFX CERES score
ZFY expression
TPM <= 2
TPM > 2 & TPM <= 5
TPM > 5 & TPM <= 10
TPM > 10 & TPM <= 50
cell lines arranged by dexcending CERES score
i
HT-1080 Cas 9:
chrX
chrY
transduction DDX3X or ZFX OE construct
HT-1080 Cas 9, DDX3X:
HT-1080 Cas 9, ZFX:
transfection: pool 18 gRNAs targeting chrY
HT-1080 Cas 9, DDX3X, iLOY:
HT-1080 Cas 9, ZFX, iLOY:
CRISPR/Cas9 depletion assay
h
Cal−120 cells (female)
PosCtrl gRNA_578 (PCNA
NegCtrl gRNA_567 (AAVS1)
ZFX-gRNA_569
ZFX-gRNA_571
percent GPF+ (gRNA−expressing) cells normalized to day 3
days after transduction
cDNA construct
Empty
ZFX
ZFY
j
HT-1080 cells (male - iLOY)
PosCtrl gRNA_579 (POLR2A)
NegCtrl gRNA_567 (AAVS1)
DDX3X_395
ZFX-gRNA_571
EIF1AX/XP1-gRNA_449
percent GPF+ (gRNA−expressing) cells normalized to day 3
days after transduction
cDNA construct
DDX3X clone 11
DDX3X clone 13
ZFX clone 2
ZFX clone 3

Figure 7

853 Figure 7: Validation of chrX-chrY paralog dependencies.

854 a) AVANA-based depletion scores (CERES) for *DDX3X,* color-coded by *DDX3Y* expression levels.
855 b) CRISPR/Cas9 depletion assay in male HT-1080 cells that carry chrY. gRNAs targeting a positive
856 control gene (*PCNA*), negative control locus (*AAVS1*), *DDX3X* (gRNA-395, gRNA-396) and *DDX3X*
857 and *DDX3Y* simultaneously are indicated. Cells were lentivirally transduced with the gRNA
858 plasmid containing GFP; GFP percentage in transduced cell line pool was measured by flow
859 cytometry at the indicated time points and normalized to day 3 post-transduction. Cells were
860 additionally transduced with empty vector (control), unrelated cDNA encoding *ZFX* (control), or
861 rescue constructs with cDNA encoding *DDX3X* or *DDX3Y*. Points in line graph represent mean,
862 and error bars denote the standard deviation (n= 3 independent experiments).
863 c) CRISPR/Cas9 depletion assay in male KNS-42 cells that lost chrY (LOY). Assay, gRNAs and cDNA
864 constructs as in (b). Points in line graph represent mean, and error bars denote the standard
865 deviation (n= 3 independent experiments).
866 d) AVANA-based depletion scores (CERES) for *EIF1AX,* color-coded by *EIF1AY* expression levels.
867 e) CRISPR/Cas9 depletion assay in male HCT 116 cells that carry chrY. gRNAs targeting positive
868 control (*PCNA*), negative control (*AAVS1*), and *EIF1AX* and *EIF1AY* simultaneously are indicated.
869 Cells were additionally transduced with empty vector (control), unrelated cDNA encoding *ZFX*
870 (control), or rescue constructs with cDNA encoding *EIF1AX* or *EIF1AY*. Assay as in (b), points in
871 line graph represent mean, and error bars denote the standard deviation (n= 3 independent
872 experiments).
873 f) CRISPR/Cas9 depletion assay in male KNS-42 cells that lost chrY (LOY). gRNAs targeting positive
874 control (*PCNA*), negative control (*AAVS1*), *EIF1AX, EIF1AX/EIF1AXP1,* and *EIF1AX/EIF1AXP1* and
875 *EIF1AY* simultaneously are indicated. Cells were additionally transduced with empty vector
876 (control) or rescue constructs with cDNA encoding *EIF1AX* or *EIF1AY*. *EIF1AX/XP1* indicates
877 *EIF1AX* and the *EIF1AXP1* pseudogene. Assay as in (b), points in line graph represent mean, and
878 error bars denote the standard deviation (n= 3 independent experiments).
879 g) AVANA-based depletion scores (CERES) for *ZFX,* color-coded by *ZFY* expression levels.
880 h) CRISPR/Cas9 depletion assay in female Cal-120 cells. gRNAs targeting positive control (*PCNA*),
881 negative control (*AAVS1*), and *ZFX* (gRNA-569, gRNA-571) are indicated. Cells were additionally
882 transduced with empty vector (control) or rescue constructs with cDNA encoding *ZFX* or *ZFY*.
883 Assay as in (b), points in line graph represent mean, and error bars denote the standard
884 deviation (n= 3 independent experiments).
885 i) Schematic depiction of workflow for induction of LOY in male HT-1080 cells expressing Cas9 and
886 DDX3X or ZFX.
887 j) CRISPR/Cas9 depletion assay in male HT-1080 cells where LOY was induced. Two clones each
888 expressing cDNA constructs encoding DDX3X or ZFX were transduced with gRNAs targeting
889 positive control (*POLR2A*), negative control (*AAVS1*), *DDX3X,* ZFX or *EIF1AX/EIF1AXP1.*
890 *EIF1AX/XP1* indicates *EIF1AX* and the *EIF1AXP1* pseudogene. Assay as in (b), points in line graph
891 represent mean, and error bars denote the standard deviation (n= 3 independent experiments).

892

893

894 **References**

895

896

897 1. Ihmels, J., Collins, S. R., Schuldiner, M., Krogan, N. J. & Weissman, J. S. Backup without redundancy:
898 genetic interactions reveal the cost of duplicate gene loss. *Mol Syst Biol* **3**, 86 (2007).

899 2. Vavouri, T., Semple, J. I. & Lehner, B. Widespread conservation of genetic redundancy during a billion
900 years of eukaryotic evolution. *Trends Genet* **24**, 485–488 (2008).

901 3. Dandage, R. & Landry, C. R. Paralog dependency indirectly affects the robustness of human cells. *Mol*
902 *Syst Biol* **15**, e8871 (2019).

903 4. Ohno, S. Evolution by Gene Duplication. (1970) doi:10.1007/978-3-642-86659-3.

904 5. Aldana, M., Balleza, E., Kauffman, S. & Resendiz, O. Robustness and evolvability in genetic regulatory
905 networks. *J Theor Biol* **245**, 433–448 (2007).

906 6. Muller, F. L. *et al.* Passenger deletions generate therapeutic vulnerabilities in cancer. *Nature* **488**,
907 337–342 (2012).

908 7. Ehrenhöfer-Wölfer, K. *et al.* SMARCA2-deficiency confers sensitivity to targeted inhibition of
909 SMARCA4 in esophageal squamous cell carcinoma cell lines. *Sci Rep-uk* **9**, 11661 (2019).

910 8. Hoffman, G. R. *et al.* Functional epigenetics approach identifies BRM/SMARCA2 as a critical synthetic
911 lethal target in BRG1-deficient cancers. *Proc National Acad Sci* **111**, 3128–3133 (2014).

912 9. Oike, T. *et al.* A Synthetic Lethality–Based Strategy to Treat Cancers Harboring a Genetic Deficiency in
913 the Chromatin Remodeling Factor BRG1. *Cancer Res* **73**, 5508–5518 (2013).

914 10. Helming, K. C. *et al.* ARID1B is a specific vulnerability in ARID1A-mutant cancers. *Nat Med* **20**, 251–
915 254 (2014).

916 11. Lelij, P. van der *et al.* Synthetic lethality between the cohesin subunits STAG1 and STAG2 in diverse
917 cancer contexts. *Elife* **6**, e26980 (2017).

918 12. Benedetti, L., Cereda, M., Monteverde, L., Desai, N. & Ciccarelli, F. D. Synthetic lethal interaction
919 between the tumour suppressor STAG2 and its paralog STAG1. *Oncotarget* **5**, 37619–37632 (2014).

920 13. Kegel, B. D., Quinn, N., Thompson, N. A., Adams, D. J. & Ryan, C. J. Comprehensive prediction of
921 synthetic lethality between paralog pairs in cancer cell lines. *BioRxiv* (2020)
922 doi:10.1101/2020.12.16.423022.

923 14. Tsherniak, A. *et al.* Defining a Cancer Dependency Map. *Cell* **170**, 564-576.e16 (2017).

924 15. Parrish, P. C. R. *et al.* Discovery of synthetic lethal and tumor suppressive paralog pairs in the human
925 genome. *Biorxiv* 2020.12.20.423710 (2020) doi:10.1101/2020.12.20.423710.

926 16. Gonatopoulos-Pournatzis, T. *et al.* Genetic interaction mapping and exon-resolution functional
927 genomics with a hybrid Cas9-Cas12a platform. *Nat Biotechnol* **38**, 638–648 (2020).

928 17. Dede, M., McLaughlin, M., Kim, E. & Hart, T. Multiplex enCas12a screens detect functional buffering
929 among paralogs otherwise masked in monogenic Cas9 knockout screens. *Genome Biol* **21**, 262 (2020).

930 18. Kegel, B. D. & Ryan, C. J. Paralog buffering contributes to the variable essentiality of genes in cancer
931 cell lines. *Plos Genet* **15**, e1008466 (2019).

932 19. Thompson, N. A. *et al.* Combinatorial CRISPR screen identifies fitness effects of gene paralogues. *Nat*
933 *Commun* **12**, 1302 (2021).

934 20. Viswanathan, S. R. *et al.* Genome-scale analysis identifies paralog lethality as a vulnerability of
935 chromosome 1p loss in cancer. *Nat Genet* **50**, 937–943 (2018).

936 21. Duijf, P. H. G., Schultz, N. & Benezra, R. Cancer cells preferentially lose small chromosomes. *Int J*
937 *Cancer* **132**, 2316–2326 (2013).

938 22. Li, C. H. *et al.* Sex differences in oncogenic mutational processes. *Nat Commun* **11**, 4330 (2020).

939 23. Wright, D. J. *et al.* Genetic variants associated with mosaic Y chromosome loss highlight cell cycle
940 genes and overlap with cancer susceptibility. *Nat Genet* **49**, 674–679 (2017).

941 24. Kaneko, S. & Li, X. X chromosome protects against bladder cancer in females via a KDM6A-
942 dependent epigenetic mechanism. *Sci Adv* **4**, eaar5598 (2018).

943 25. Spatz, A., Borg, C. & Feunteun, J. X-Chromosome Genetics and Human Cancer. *Nat Rev Cancer* **4**,
944 617–629 (2004).

945 26. Hunter, S., Gramlich, T., Abbott, K. & Varma, V. Y chromosome loss in esophageal carcinoma: An in
946 situ hybridization study. *Genes Chromosomes Cancer* **8**, 172–177 (1993).

947 27. Agahozo, M. C. *et al.* Loss of Y-Chromosome during Male Breast Carcinogenesis. *Cancers* **12**, 631
948 (2020).

949 28. Minner, S. *et al.* Y chromosome loss is a frequent early event in urothelial bladder cancer. *Pathology*
950 **42**, 356–359 (2010).

951 29. Lin, S.-H. *et al.* Mosaic chromosome Y loss is associated with alterations in blood cell counts in UK
952 Biobank men. *Sci Rep-uk* **10**, 3655 (2020).

953 30. Forsberg, L. A. *et al.* Mosaic loss of chromosome Y in peripheral blood is associated with shorter
954 survival and higher risk of cancer. *Nat Genet* **46**, 624–628 (2014).

955 31. Thompson, D. J. *et al.* Genetic predisposition to mosaic Y chromosome loss in blood. *Nature* **575**,
956 652–657 (2019).

957 32. Guo, X. *et al.* Mosaic loss of human Y chromosome: what, how and why. *Hum Genet* **139**, 421–446
958 (2020).

959 33. Lau, Y.-F. C. Y chromosome in health and diseases. *Cell Biosci* **10**, 97 (2020).

960 34. Shi, J. *et al.* Discovery of cancer drug targets by CRISPR-Cas9 screening of protein domains. *Nat*
961 *Biotechnol* **33**, 661–7 (2015).

962 35. Dass, B. *et al.* Loss of polyadenylation protein τCstF-64 causes spermatogenic defects and male
963 infertility. *Proc National Acad Sci* **104**, 20374–20379 (2007).

964 36. Romeo, V., Griesbach, E. & Schümperli, D. CstF64: Cell Cycle Regulation and Functional Role in 3' End
965 Processing of Replication-Dependent Histone mRNAs. *Mol Cell Biol* **34**, 4272–4284 (2014).

966 37. Yao, C. *et al.* Overlapping and distinct functions of CstF64 and CstF64τ in mammalian mRNA 3'
967 processing. *Rna* **19**, 1781–1790 (2013).

968 38. Minvielle-Sebastia, L., Winsor, B., Bonneaud, N. & Lacroute, F. Mutations in the yeast RNA14 and
969 RNA15 genes result in an abnormal mRNA decay rate; sequence analysis reveals an RNA-binding domain
970 in the RNA15 protein. *Mol Cell Biol* **11**, 3075–3087 (1991).

971 39. Mohr, S. E., Smith, J. A., Shamu, C. E., Neumüller, R. A. & Perrimon, N. RNAi screening comes of age:
972 improved techniques and complementary approaches. *Nat Rev Mol Cell Bio* **15**, 591–600 (2014).

973 40. Meyers, R. M. *et al.* Computational correction of copy number effect improves specificity of CRISPR–
974 Cas9 essentiality screens in cancer cells. *Nat Genet* **49**, 1779–1784 (2017).

975 41. Behan, F. M. *et al.* Prioritization of cancer therapeutic targets using CRISPR–Cas9 screens. *Nature*
976 **568**, 511–516 (2019).

977 42. McDonald, E. R. *et al.* Project DRIVE: A Compendium of Cancer Dependencies and Synthetic Lethal
978 Relationships Uncovered by Large-Scale, Deep RNAi Screening. *Cell* **170**, 577-592.e10 (2017).

979 43. Nusinow, D. P. *et al.* Quantitative Proteomics of the Cancer Cell Line Encyclopedia. *Cell* **180**, 387-
980 402.e16 (2020).

981 44. Ghandi, M. *et al.* Next-generation characterization of the Cancer Cell Line Encyclopedia. *Nature* **569**,
982 503–508 (2019).

983 45. Fortin, J.-P. *et al.* Multiple-gene targeting and mismatch tolerance can confound analysis of genome-
984 wide pooled CRISPR screens. *Genome Biol* **20**, 21 (2019).

985 46. Nijhawan, D. *et al.* Cancer Vulnerabilities Unveiled by Genomic Loss. *Cell* **150**, 842–854 (2012).

986 47. Paolella, B. R. *et al.* Copy-number and gene dependency analysis reveals partial copy loss of wild-
987 type SF3B1 as a novel cancer vulnerability. *Elife* **6**, e23268 (2017).

988 48. Oughtred, R. *et al.* The BioGRID database: A comprehensive biomedical resource of curated protein,
989 genetic, and chemical interactions. *Protein Sci* **30**, 187–200 (2021).

990 49. Modos, D. *et al.* Identification of critical paralog groups with indispensable roles in the regulation of
991 signaling flow. *Sci Rep-uk* **6**, 38588 (2016).

992 50. Neggers, J. E. *et al.* Synthetic Lethal Interaction between the ESCRT Paralog Enzymes VPS4A and
993 VPS4B in Cancers Harboring Loss of Chromosome 18q or 16q. *Cell Reports* **33**, 108493 (2020).

994 51. Szymańska, E. *et al.* Synthetic lethality between VPS4A and VPS4B triggers an inflammatory response
995 in colorectal cancer. *Embo Mol Med* **12**, e10812 (2020).

996 52. Wu, J. *et al.* Cryo-EM Structure of the Human Ribonuclease P Holoenzyme. *Cell* **175**, 1393-1404.e11
997 (2018).

998 53. Welting, T. J. M., Kikkert, B. J., Venrooij, W. J. van & Pruijn, G. J. M. Differential association of protein
999 subunits with the human RNase MRP and RNase P complexes. *Rna* **12**, 1373–1382 (2006).

1000 54. GUERRIER-TAKADA, C., EDER, P. S., GOPALAN, V. & ALTMAN, S. Purification and characterization of
1001 Rpp25, an RNA-binding protein subunit of human ribonuclease P. *Rna* **8**, 290–295 (2002).

1002 55. Goldfarb, K. C. & Cech, T. R. Targeted CRISPR disruption reveals a role for RNase MRP RNA in human
1003 preribosomal RNA processing. *Gene Dev* **31**, 59–71 (2017).

1004 56. Jones, P. A. Functions of DNA methylation: islands, start sites, gene bodies and beyond. *Nat Rev*
1005 *Genet* **13**, 484–492 (2012).

1006 57. Tukiainen, T. *et al.* Landscape of X chromosome inactivation across human tissues. *Nature* **550**, 244–
1007 248 (2017).

1008 58. Balaton, B. P., Cotton, A. M. & Brown, C. J. Derivation of consensus inactivation status for X-linked
1009 genes from genome-wide studies. *Biol Sex Differ* **6**, 35 (2015).

1010 59. Dunford, A. *et al.* Tumor-suppressor genes that escape from X-inactivation contribute to cancer sex
1011 bias. *Nat Genet* **49**, 10–16 (2016).

1012 60. Wernitznig, A. *et al.* Abstract 3227: CLIFF, a bioinformatics software tool to explore molecular
1013 differences between two sets of cancer cell lines. 3227–3227 (2020) doi:10.1158/1538-7445.am2020-
1014 3227.

1015 61. Sekiguchi, T., Iida, H., Fukumura, J. & Nishimoto, T. Human DDX3Y, the Y-encoded isoform of RNA
1016 helicase DDX3, rescues a hamster temperature-sensitive ET24 mutant cell line with a DDX3X mutation.
1017 *Exp Cell Res* **300**, 213–222 (2004).

1018 62. Wang, T. *et al.* Identification and characterization of essential genes in the human genome. *Science*
1019 **350**, 1096–1101 (2015).

1020 63. Zuo, E. *et al.* CRISPR/Cas9-mediated targeted chromosome elimination. *Genome Biol* **18**, 224 (2017).

1021 64. Adikusuma, F., Williams, N., Grutzner, F., Hughes, J. & Thomas, P. Targeted Deletion of an Entire
1022 Chromosome Using CRISPR/Cas9. *Mol Ther* **25**, 1736–1738 (2017).

1023 65. Fong, P. C. *et al.* Inhibition of Poly(ADP-Ribose) Polymerase in Tumors from BRCA Mutation Carriers.
1024 *New Engl J Medicine* **361**, 123–134 (2009).

1025 66. Bryant, H. E. *et al.* Specific killing of BRCA2-deficient tumours with inhibitors of poly(ADP-ribose)
1026 polymerase. *Nature* **434**, 913–917 (2005).

1027 67. Farmer, H. *et al.* Targeting the DNA repair defect in BRCA mutant cells as a therapeutic strategy.
1028 *Nature* **434**, 917–921 (2005).

1029 68. Godfrey, A. K. *et al.* Quantitative analysis of Y-Chromosome gene expression across 36 human
1030 tissues. *Genome Res* **30**, 860–873 (2020).

1031 69. Venkataramanan, S., Calviello, L., Wilkins, K. & Floor, S. N. DDX3X and DDX3Y are redundant in
1032 protein synthesis. *Biorxiv* 2020.09.30.319376 (2020) doi:10.1101/2020.09.30.319376.

1033 70. Szappanos, D. *et al.* The RNA helicase DDX3X is an essential mediator of innate antimicrobial
1034 immunity. *Plos Pathog* **14**, e1007397 (2018).

1035 71. Michlits, G. *et al.* Multilayered VBC score predicts sgRNAs that efficiently generate loss-of-function
1036 alleles. *Nat Methods* 1–9 (2020) doi:10.1038/s41592-020-0850-8.

1037 72. Li, W. *et al.* MAGeCK enables robust identification of essential genes from genome-scale
1038 CRISPR/Cas9 knockout screens. *Genome Biol* **15**, 554 (2014).

1039 73. Li, H. *et al.* The Sequence Alignment/Map format and SAMtools. *Bioinformatics* **25**, 2078–2079
1040 (2009).

1041 74. Hofmann, M. H. *et al.* BI-3406, a potent and selective SOS1::KRAS interaction inhibitor, is effective in
1042 KRAS-driven cancers through combined MEK inhibition. *Cancer Discov* CD-20-0142 (2020)
1043 doi:10.1158/2159-8290.cd-20-0142.

1044 75. Colaprico, A. *et al.* TCGAbiolinks: an R/Bioconductor package for integrative analysis of TCGA data.
1045 *Nucleic Acids Res* **44**, e71–e71 (2016).

1046 76. Li, Y., Ge, D. & Lu, C. The SMART App: an interactive web application for comprehensive DNA
1047 methylation analysis and visualization. *Epigenet Chromatin* **12**, 71 (2019).

1048 77. Bengtsson, H., Simpson, K., Bullard, J. & Hansen, K. aroma.affymetrix: A generic framework in R for
1049 analyzing small to very large Affymetrix data sets in bounded memory. *Report 745, Department of*
1050 *Statistics, University of California, Berkeley, 2008* (2008).

1051 78. Mayrhofer, M., Viklund, B. & Isaksson, A. Rawcopy: Improved copy number analysis with Affymetrix
1052 arrays. *Sci Rep-uk* **6**, 36158 (2016).

1053 79. Greenman, C. D. *et al.* PICNIC: an algorithm to predict absolute allelic copy number variation with
1054 microarray cancer data. *Biostatistics* **11**, 164–175 (2010).

1055 80. Hörmann, A. *et al.* RIOK1 kinase activity is required for cell survival irrespective of MTAP status.
1056 *Oncotarget* **9**, 28625–28637 (2018).

1057 81. Hu, Y. *et al.* An integrative approach to ortholog prediction for disease-focused and other functional
1058 studies. *Bmc Bioinformatics* **12**, 357 (2011).

1059 82. Chen, W.-H., Lu, G., Chen, X., Zhao, X.-M. & Bork, P. OGEE v2: an update of the online gene
1060 essentiality database with special focus on differentially essential genes in human cancer cell lines.
1061 *Nucleic Acids Res* **45**, D940–D944 (2016).

1062